Title

Common Gene Networks Orchestrate Organelle Architecture and Inter-Organelle Metabolic Flows for Mucin Production in High Endothelial and Goblet Cells

Yuhan Bi[1,2,3,6*], Kevin Brulois[1,2,3], Aiman Ayesha[1,2,3], Menglan Xiang[1,2,3], Romain Ballet[1,2,3], Borja Ocón[1,2,3], Theresa Dinh[2,3], Nicole Lazarus[2,3], Manali Kunte[2,3], Yongzhi Wang[1,2,3], Evan Bao[1,2,3], Griselda Ramos[2,3], Florea Lupu[4], Jonathan H Lin[1,2,3], Eugene C. Butcher[1,2,3**#] and Junliang Pan [2,3***#].

1 Department of Pathology, Stanford University School of Medicine, Stanford, CA, USA. 2 Palo Alto Veterans Institute for Research, Palo Alto, CA, USA. 3 Veterans Affairs Palo Alto Health Care System, Palo Alto, CA, USA. 4 Okahoma Medical Research Foundation, Oklahoma City, OK, USA.

6 Lead Contact

Co-senior Authors

* Correspondence. Email: yub10@stanford.edu, ebutcher@stanford.edu, jpan@stanford.edu

Graphic Abstract

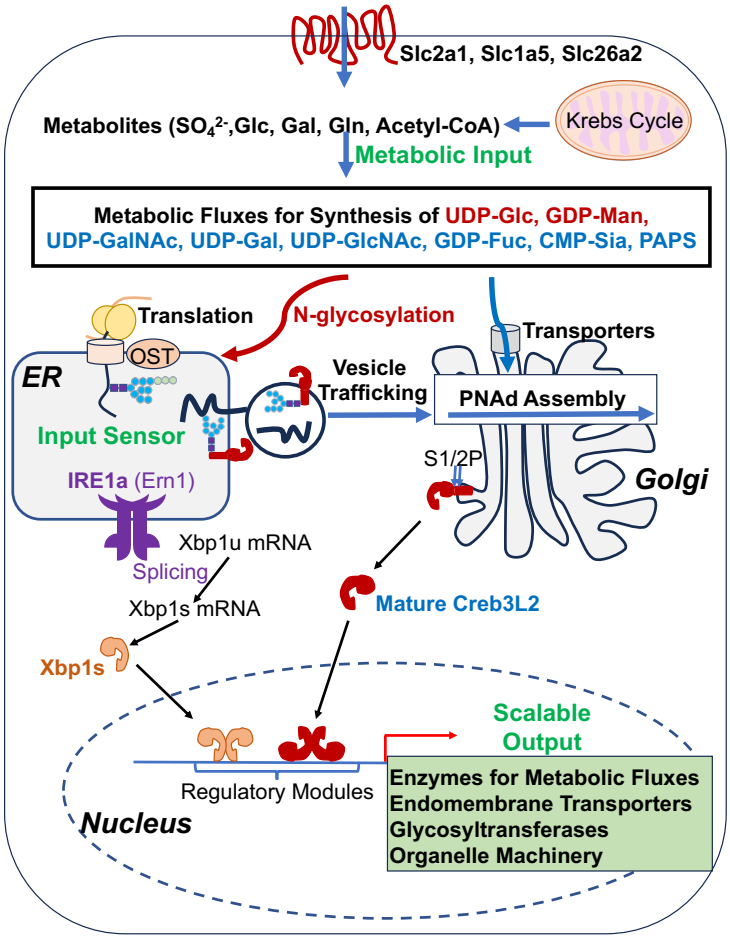

Key points

- Sulfated O-glycan biosynthesis is coordinated through the integration of inter-organelle metabolic fluxes with organellar protein machineries in HECs and GCs.
- IRE1α-XBP1 and CREB3L1/2 coordinate gene networks that orchestrate this integration in HECs and GCs.
- Inhibiting XBP1 or CREB3L2 activation flattens HECs, reduces PNAd expression, and diminishes lymphocyte homing.
- XBP1 deletion disrupts metabolic fluxes required for PNAd synthesis, impairing HEC morphology, lymphocyte recruitment, and ectopic induction during inflammation.

Keywords

High endothelial cells, Goblet cells, Lineage specific secretory cell, Inter-organelle metabolic fluxes, Sulfated mucin type O-glycan specialization, Organellar architecture, Gene regulatory network, Lymphocyte trafficking, Mucosal immunity, Immunometabolism.

Summary

High endothelial cells (HECs) and intestinal goblet cells (GCs) are highly specialized through organelle expansion and metabolism for production of sulfated mucins essential for lymphocyte homing and mucosal defense, respectively. How these cells coordinate organelle architecture and biosynthetic pathways to support such demands remains poorly understood. Here, we show at single-cell resolution that HECs rely on gene regulatory networks driven by IRE1α-XBP1 and CREB3L1/2 transcription factors. These networks upregulate enzymes and transporters that control inter-organelle metabolic fluxes for the step-wise assembly of sulfated O-glycan synthesis, while scaling the endoplasmic reticulum (ER) and Golgi apparatus, reinforcing cargo trafficking and organizing sequential glycosyltransferase deployment. Genetic and pharmacological perturbations show that these transcriptional circuits sustain lymph node HEC morphology and function in lymphocyte homing, and drive ectopic induction of HEV during inflammation. Parallel transcriptional networks operate in GCs. Together, our findings define a conserved regulatory logic that integrates metabolic pathways and organelle architecture to enable committed sulfo-mucin cell specialization across distinct tissue contexts.

Introduction

All eukaruotic cells assimilate nutrients and convert metabolic intermediates into macromolecules to establish their morphology, function, and identity. Yet how cells logistically and mechanistically coordinate metabolic fluxes—the directional flow of metabolites through biochemical networks—to fuel specialized architecture and function remains a central unresolved question in cell biology[1,2]**.** This challenge is particularly acute in the context of the immune responses, where challenged immune, stromal and barrier epithelial cells must remain highly adaptable to context and demand[3-5].

High endothelial cells (HECs) exemplify this biological challenge. These specialized endothelial cells line high endothelial venules (HEVs) in lymph nodes (LNs) and can be induced de novo sites of chronic inflammation and tumors, where they uniquely support blood-borne lymphocyte recruitment. This process is driven by the binding of the lymphocyte homing receptors to peripheral node addressin (PNAd)[6,7], selectively expressed by HECs. PNAd comprises HEV cell surface sialomucins that are densely elaborated with O-glycans bearing 6-sulfo sialyl Lewis X (6-sulfo sLe^X), the high affinity carbohydrate ligand for the lymphocyte homing receptor L-selectin[8,9]. The synthesis of PNAd is metabolically intensive and spatially orchestrated, and it correlates with the striking cuboidal morphology of HEC marked by expanded ER, Golgi, polyribosomes, and mitochondria[10,11]. Intestinal goblet cells (GCs), which like HECs are factories for heavily O-glycosylated mucin production, share similar coordinated organelle expansion[12], suggesting conserved principles coordinating the integration of metabolism, organelle architecture, and function.

PNAd$^+$ HECs are not confined to lymph nodes but can be induced in diverse settings of chronic inflammation[13], including persistent infection, autoimmunity, graft rejection, and cancer. PNAd$^+$ HECs induction in non-lymphoid tissues correlates with lymphocyte infiltration[14,15]. This process depends on lymphotoxin signaling[16] and noncanonical NF-κB activation[17], which are required for HEV induction and maintenance both in secondary and tertiary lymphoid structures[18]. However, these pathways do not explain how HECs simultaneously acquire their distinct cuboidal morphology and biosynthetic capacity for PNAd expression. Despite their immunological importance, we lack a coherent framework to explain how these cells are programmed.

Unlike template-driven processes such as transcription or translation, PNAd biosynthesis is governed by the integrated engagement of metabolic fluxes[8,19]. It requires: (1) sustained production of nucleotide-activated sugar donors and 3′-phosphoadenosine 5′-phosphosulfate (PAPS); (2) coordinated transport of these substrates from the cytosol into the Golgi lumen; and (3) precise spatial and temporal control of glycosyltransferases and sulfotransferases across Golgi cisternae[20]. Although individual steps in sulfoglycan synthesis have been characterized, how metabolic fluxes are tuned across organelles *in vivo*—and how these fluxes are transcriptionally programmed to shape lineage-specific cell states—remains poorly understood.

Here, we show that two conserved basic leucine zipper transcription factors (bZIP TFs)—XBP1[21,22] and CREB3L2[23,24]—coordinately drive an integrated gene regulatory network (GRN) that directly couples ER and Golgi function to the inter-organelle metabolic fluxes essential for PNAd biosynthesis. During the unfolded protein response (UPR), Xbp1 is activated through IRE1α-mediated unconventional splicing of its mRNA[21,22], while Creb3l2 is activated by regulated intramembrane proteolysis in the Golgi[23,24]. These factors cooperate in driving secretory capacity, yet little is known about their role in coordinating metabolic flow between organelles. By integrating single-cell transcriptomics, comparative and phylogenomic analysis, we reveal that the IRE1α–XBP1- and CREB3L2-driven GRNs are essential for the metabolic and architectural specialization of HECs and GCs. These networks enhance ER and Golgi throughput, upregulate metabolic pathways for nucleotide sugar and PAPS synthesis, promote their transport from the cytosol into the Golgi lumen, spatially coordinate glycosyltransferase deployment to ensure efficient PNAd assembly, and sustain organelle architecture. Biochemical, pharmacological, and genetic perturbations demonstrate that these GRNs are necessary not only for PNAd biosynthesis and lymphocyte homing, but also for the ectopic emergence and functional remodeling of HECs during inflammation. We further identify a comparable integrated network in intestinal GCs that couples inter-organelle metabolic fluxes for glycosylation with secretory organelle architecture and function.

Together, our findings establish IRE1α–XBP1 and CREB3L2 as central nodes in a transcriptional program that orchestrates inter-organelle metabolic fluxes to drive secretory cell specialization. This work uncovers a conserved regulatory logic linking metabolism, organelle architecture, and critical immune system functions in mucin producing endothelial and epithelial cells.

Results

Gene Networks Link PNAd Biosynthesis to Organelle Expansion and the ‘High’ Endothelial Phenotype

The biosynthesis of PNAd-bearing mucins, a defining feature of high endothelial cells (HECs), requires sustained metabolic input and specialized organelle machinery, the expansion of which underlies the characteristic 'high' endothelial morphology[25-27]. To define the metabolic programs supporting this process, we analyzed single-cell transcriptomes of murine lymph node (LN) endothelial subsets[26] (Suppl. Fig. 1A). Differential expression analysis revealed that HECs uniquely upregulate a suite of genes required for PNAd biosynthesis, including nutrient transporters, metabolic enzymes for precursor synthesis, Golgi-resident transporters, glycosyltransferases and sulfotransferases that mediate stepwise glycan assembly (Fig. 1A, Suppl. Fig. 1B-C). Among the top 2,000 differentially expressed genes (DEGs) enriched in HECs relative to other endothelial subsets, nearly all key regulators of the metabolic fluxes required for PNAd synthesis were represented (Fig. 1A–C, DEG list provided in Table S1). These findings indicate that HECs transcriptionally scale metabolic pathways to meet the biosynthetic demands of PNAd production.

These upregulated metabolic gene programs encompass every critical step of PNAd biosynthesis, from precursor generation to glycan assembly (Fig. 1B). PNAd glycans, including the 6-sulfo sialyl Lewis X (6-sulfo SLe^X) carbohydrate ligands for the lymphocyte homing receptor L-selectin, are assembled within the Golgi apparatus from nucleotide sugar and sulfate donors. HEC-enriched genes support the generation of these donors via multiple cytosolic pathways. The hexosamine biosynthetic pathway (HBP) generates UDP-GlcNAc and UDP-GalNAc from glucose, galactose, and glutamine through the actions of Gfpt1, Pgm3, Uap1, and Gale, relying on nutrient uptake (via SLC2A1, SLC1A5) and acetyl-CoA derived from mitochondrial fatty acid β-oxidation and the citrate-malate-pyruvate shuttle[19,28,29]. Additional donors—including UDP-Gal, CMP-Neu5Ac, GDP-Fuc, and PAPS—are synthesized via the Leloir, sialic acid, fucose and sulfate donor pathways[19,30,31], with specialized Golgi-resident transporters (e.g., Slc35a1, Slc35b2/3, Slc35c1) directing these precurcors into the Golgi lumen for glycan assembly[32]. PNAd biosynthesis initiates at cis-Golgi with Galnt12-mediated transfer of GalNAc to mucin core proteins such as Glycam1, CD34, Parm1, Podocalyxin, and CD24, followed by the stepwise action of glycosyltransferases and sulfotransferases including C1galt1, Gcnt1, B3gnt3, Fut7, Chst4, and St3gal4[8,25], along the Golgi stacks.

The 'high' endothelial morphology of HEC derives from the expansion of polyribosomes, ER, Golgi, mitochondria, and autophagolysosomal systems, providing the architectural framework for glyco-mucin synthesis and inter-organelle precursor flow. Alongside metabolic flux, HECs upregulate gene programs required for the generation and function of organelles that support high-output glycoprotein production (Fig. 1D–F). HEC-enriched genes include those for ER-targeted protein translation, translocation and cotranslational N-glycosylation (Ssr1, Sec61b, Spcs2, Rpn1, Dpagt1, Alg2, Stt3a, Stt3b, Ost4, Tmem258, Ddost)[33], ER chaperones (Hspa5, Calr, Canx, Dnajb9, Pdia3, Pdia6)[34], and ER-associated degradation (Edem2, Derl1, Os9, Erlec1, Vcp, Syvn1)[35]. Cargo trafficking is coordinated by COPII components (Mia3, Lman1, Sar1b, Sec23b, Sec24d)[36] and COPI machinery (Kdelr1, Arf3, Copb2)[37], while Golgi organization relies on scaffold proteins such as Golga2, Golgb1, and Golph3[38]. Additional HEC-enriched programs support mitochondrial fatty acid oxidation and citrate shuttling (Mpc1, Cpt1a, Acad10, Slc25a1, Acly)[39] and membrane maintenance and autophagy (Apoe, Agpat5, Lamp1, Becn1)[40], highlighting tight coordination between energy metabolism and organelle function.

The expansive upregulation of these biosynthetic metabolic and organelle programs is associated with expression of transcriptional regulators of the UPR. HECs show marked enrichment of the IRE1α-XBP1 arm of the UPR, including Ern1 (IRE1α), spliced Xbp1, and their effector Creb3l2, together with the proteases Mbtps1 and Mbtps2 required for CREB3L2 activation. In contrast, the PERK-ATF4 branch is selectively suppressed in HECs, as indicated by low Atf4 expression and elevated Dnajc3, an inhibitor of PERK signaling[41]. While both branches reduce ER stress, XBP1 drives an adaptive anabolic program that reacts to ER stress by expanding ER and secretory machinery[42]. In contrast, PERK broadly represses global translation to reduce ER load[21]. The selective engagement of IRE1α-XBP1 and CREB3L2, together with PERK suppression, likely

supports the continuous metabolic flux and organelle scaling required for PNAd synthesis and lymphocyte recruitment, defining the specialized 'high' endothelial state.

Taken together, these single-cell resolution findings demonstrate that the inter-organelle metabolic processes driving PNAd synthesis are intricately coupled with the protein machineries of organelles, reinforcing the distinctive ‘high’ cuboidal morphology of HECs as well as their unique biochemical and functional features.

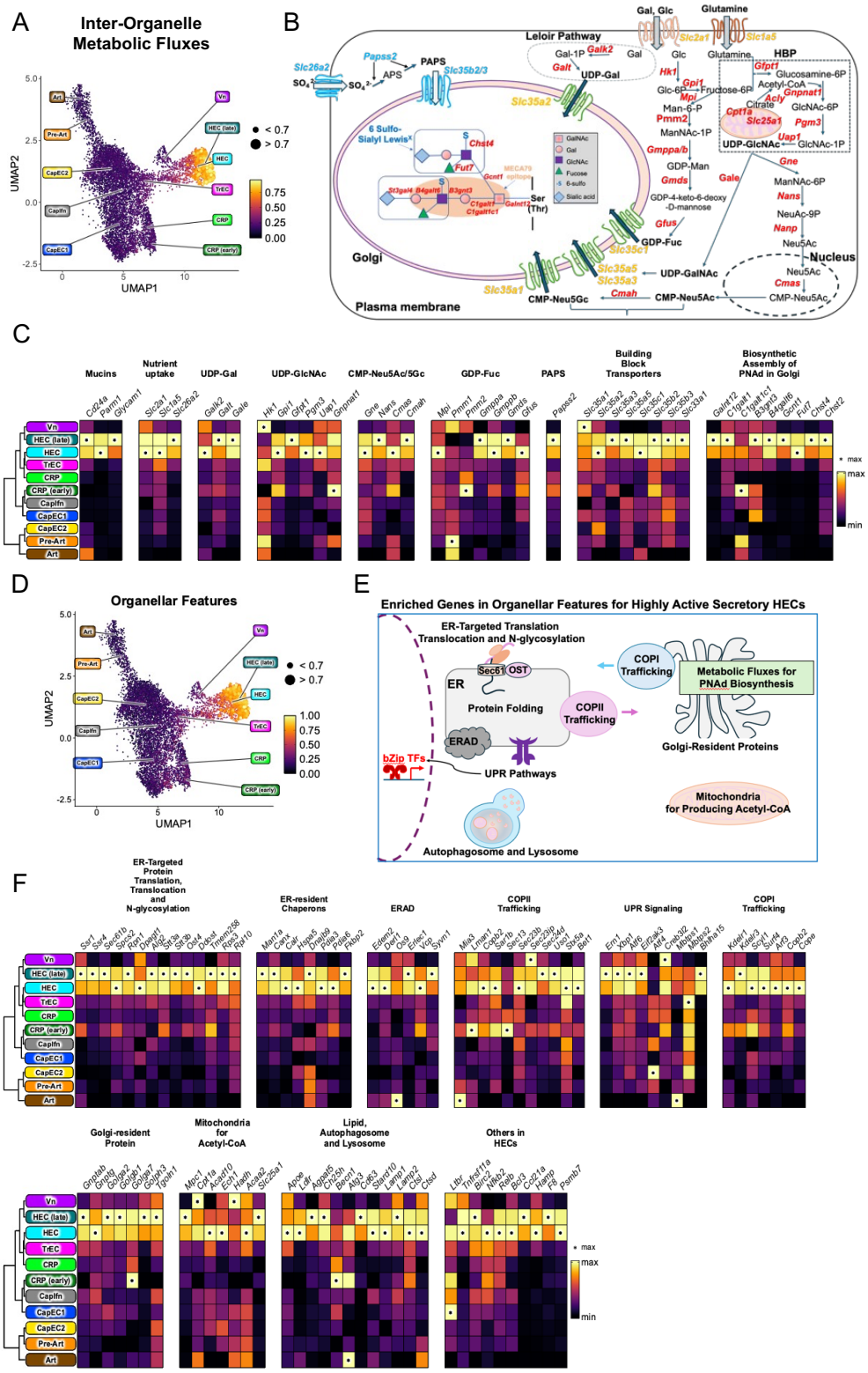

Fig. 1 Gene Networks Link PNAd Biosynthesis to Organelle Expansion and the 'High' Endothelial Phenotype.
A. UMAP projection of scRNA-seq data from murine peripheral LN ECs[26], showing module scores that summarize the expression levels of genes controlling metabolic fluxes for PNAd synthesis in HECs compared to other EC subsets. Mean expression profiles of the genes used for these module scores are provided in C.

B. A schematic chart depicts the genes and flow of metabolic fluxes, starting with nutrient uptake and building block production, followed by their transport into the Golgi lumen, and culminating in the stepwise assembly of PNAd[8] on mucins within Golgi stacks. Transporters and enzymes involved in each step are color-coded in yellow and red, respectively, with those specifically involved in sulfation shown in blue.
C. Heat maps showing the enriched expression of genes in HECs that coordinate metabolic fluxes essential for PNAd biosynthesis.
D. UMAP projection of scRNA-seq data from murine peripheral LN ECs, showing module scores that summarize the expression levels of genes controlling organellar features. Mean expression profiles of the genes used for these module scores are provided in F.
E. Schematic chart illustrates the organellar protein machineries and their functions that shape the distinctive "high" cuboidal morphology of HECs.
F. Heat maps illustrate the HEC-enriched expression of genes associated with organellar structures and their functions.
Mean expression values in panels C and F are derived from three independent samples and are shown on a color scale from min to max, with an asterisk (*) indicating the maximum value.

Goblet Cells Share Gene Programs with HECs to Drive Sulfated Mucin Production and Organelle Expansion

Intestinal goblet cells (GCs) deploy sulfated mucins that form a key component of the mucosal barrier. Sulfation is directed by CHST4, a sulfotransferase also required for PNAd biosynthesis in HECs[43]. We asked whether GCs employ similar molecular pathways to couple sulfated mucin synthesis with organelle function, by analysing single-cell RNA sequencing data from mouse intestinal epithelial cells in the Tabula Muris atlas[44]. As shown in Suppl. Fig. 2A, GCs exhibit a strikingly similar molecular profile, sharing virtually all sets of genes involved in the inter-organelle metabolic processes that drive sulfated O-glycan production on mucins (Suppl. Fig. 2A and B). They also display enhanced expression of genes for ER- and Golgi-resident protein machineries that coordinate and streamline cargo trafficking along the secretory pathway (Suppl. Fig. 2C). Finally, GCs appear to engage analogous regulatory mechanisms, characterized by enriched expression of the Ern2-Xbp1 signaling axis[45], the transcription factors Creb3l1 and Creb3l2[44], and the intramembrane proteases Mbtps1 and Mbtps2[46]. These data suggest that GCs and HECs leverage shared regulatory networks to couple metabolic flux with organelle expansion for high-output glycosylation.

XBP1 and CREB3L2 Direct Conserved Gene Networks Integrating PNAd Synthesis and Organelle Scaling

Having identified a shared metabolic and organellar gene program in HECs and GCs, we next sought to define the upstream regulatory networks that drive this convergence. Gene set overlap analysis across endothelial and intestinal epithelial subsets revealed that HECs and GCs share a highly correlated transcriptional signature (Fig. 2A). Among the top 2,000 DEGs enriched in HECs, 346 were co-upregulated in GCs, the majority of which encode components of metabolic flux pathways and organellar protein machineries (Suppl. 2B and C). This overlap suggests that a common set of *cis*- and *trans*-acting factors underlies their shared transcriptional architecture.

To identify candidate upstream transcription factors (TFs), we performed enrichment analysis on these 346 shared genes using the Enrichr platform[47,48]. Across multiple datasets—including TF perturbation signatures, co-expression networks, and curated TF-gene associations—XBP1 and CREB3/CREB3L2 consistently emerged as the top regulatory candidates (Fig. 2B, Suppl. Fig. 3A, Table S2). Independent analyses of HEC- and GC-specific gene sets further supported a central role for XBP1 and CREB3L2 in

coordinating the metabolic and organellar programs that enable sulfated mucin biosynthesis (Suppl. Fig. 3B–C, Table S3-4).

To examine potential cis-regulatory elements mediating this control, we performed de novo motif discovery on HEC-enriched genes. We focused on highly conserved non-coding regions—including promoters, gene bodies, and 5 kb flanking sequences—identified by phastCons placental mammal conservation scores from the UCSC Genome Browser[49-51]. Using the HOMER platform[52], we identified bZIP family binding sites, including a consensus sequence recognized by XBP1 and CREB3L2 (t/cg/t/ACGTc/aA), among the top enriched motifs (Fig. 2C). Comparative phylogenomic analysis using Multiz alignments from 58 eutherian mammals and PhyloP conservation scores confirmed the presence of XBP1 and CREB3L2 binding sites within conserved non-coding elements across multiple sets of genes involved in PNAd synthesis of HEC, sulfated mucin in the GC, and organellar machinery regulation (Fig. 2D, Data S1). These XBP1 and CREB3L2 binding sites frequently co-occurred with binding motifs for other regulatory factors, including E-box, ETS, KLF/Sp1, NFYA/B, and NF-κB, suggesting that XBP1- and CREB3L2-driven gene regulatory networks may interface with additional lineage- and state-specific programs.

Collectively, these analyses identified XBP1 and CREB3L2 as candidate transcriptional regulators of the metabolic and organellar gene programs shared between HECs and GCs. Their conserved binding motifs across sulfated mucin biosynthesis and organelle scaling genes suggest a model in which these factors directly coordinate secretory specialization through cis-regulatory modules embedded within the mammalian genome.

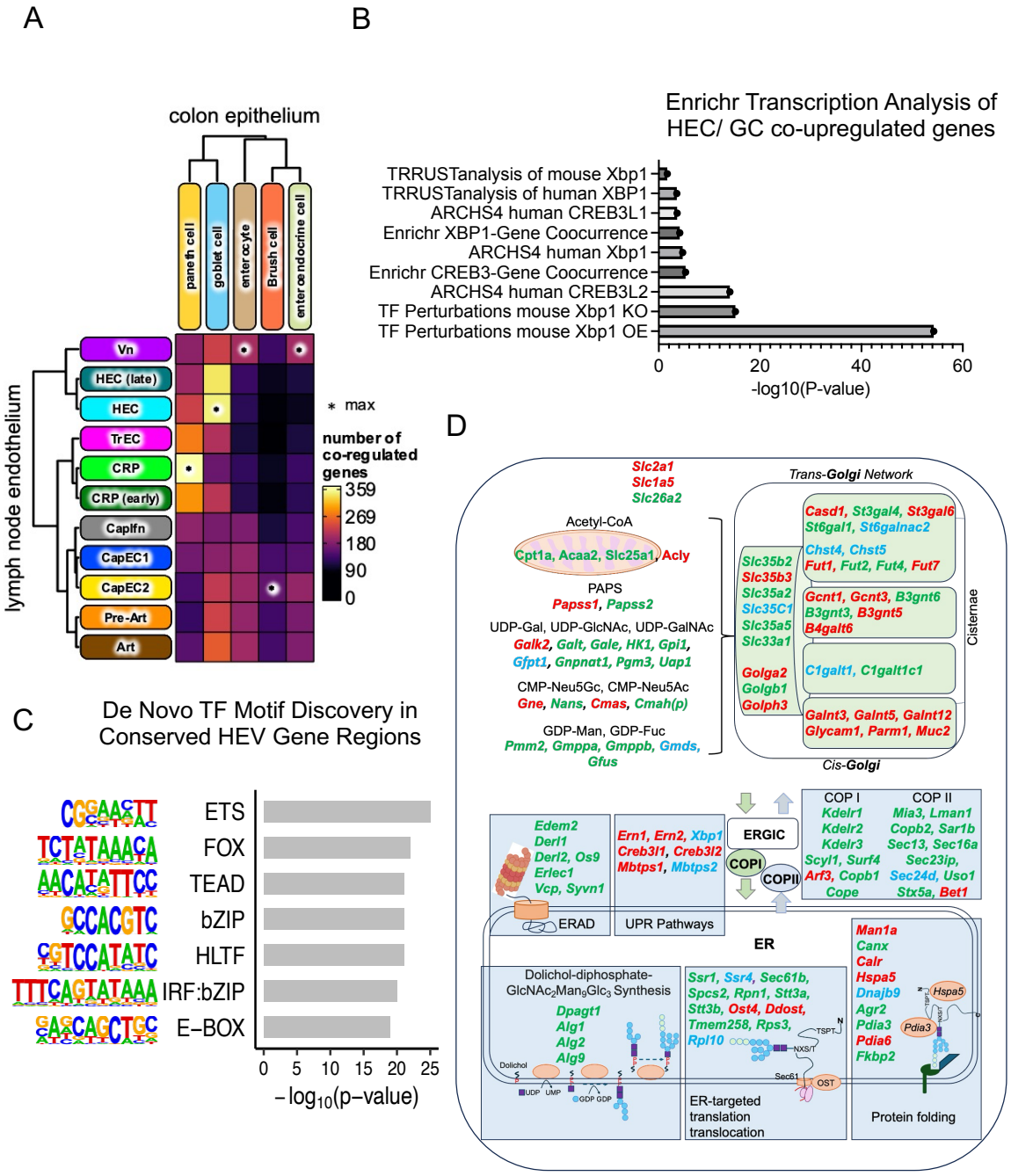

Fig. 2. XBP1 and CREB3L2 Direct Conserved Gene Networks Integrating PNAd Synthesis and Organelle Scaling.
A. Gene set overlap of DEGs (top 2000 DEGs for individual cell subsets, computed independently for lymph node endothelium and intestinal epithelium) revealed that HECs and GCs share a highly correlated transcriptional signature enriched for genes involved in integrating sulfated O-glycan synthesis with organellar machineries.
B. Transcription factor enrichment analysis of the 346 co-upregulated genes shared between HECs and GCs identified XBP1 and CREB3/CREB3L2 as top candidate regulators. Enrichment was performed using the Enrichr platform, drawing from the indicated datasets (Link of 346 shared genes in Table S2). Also see Suppl. Fig. 3.
C. De novo motif discovery in conserved regulatory regions flanking HEC-enriched genes identified bZIP family binding sites, including the consensus sequence for XBP1 and CREB3L2. Motif analysis was performed using HOMER on the mouse mm10 genome, with conserved regions defined by phastCons placental mammal scores.
D. Phylogenetic footprinting revealed evolutionarily conserved XBP1- and CREB3L2-binding motifs within regulatory elements of genes involved in PNAd biosynthesis and organellar function. Genes containing CREB3L2 motifs (TGAN$_{1-2}$TCA) are shown in red, XBP1/ CREB3L2 motifs ("ACGTG") in green, and genes with both motifs in blue.

XBP1 and CREB3L2 Drive Gene Expression from Conserved Enhancer/Promoter Elements of PNAd Biosynthetic genes

Having identified conserved XBP1 and CREB3L2 binding motifs across genes involved in PNAd biosynthesis and organelle function, we next tested whether these motifs and transcription factors could directly regulate gene expression. We focused on glycosyltransferases and nucleotide sugar biosynthetic enzymes localized to the Golgi and cytosol, including *Chst4* (sulfation), *Fut7* (fucosylation), *C1galt1* (core 1 O-glycan synthesis), *Pgm3* (UDP-GalNAc production via the hexosamine biosynthetic pathway)[53], and *Nans* (CMP-Neu5Ac synthesis)[54] (Fig. 3A).

To assess direct transcriptional regulation, we generated luciferase reporter constructs driven by isolated enhancer and promoter regions from these genes, containing the evolutionarily conserved XBP1 and/or CREB3L2 binding sites identified in our motif analysis. ATAC-seq analysis of sorted peripheral LN HECs confirmed that these regions exhibit open chromatin states (data not shown). Electrophoretic mobility shift assays (EMSAs) demonstrated site-specific binding of recombinant spliced XBP1 (XBP1s) or active CREB3L2 to these motifs (Suppl. Fig. 4A-B).

Transient transfection-based reporter assays in 293T cells revealed that overexpression of IRE1α, Xbp1s, or active form of CREB3L2 significantly transactivated the *Chst4* enhancer-promoter, whereas an IRE1α dominant-negative mutant (IRE1-Mut) or unspliced Xbp1 showed markedly reduced activity. Co-expression of Xbp1s and CREB3L2 elicited enhanced activation, indicating cooperative control of *Chst4* transcription by these two regulatory arms (Fig. 3C).

Interestingly, the *Fut7* promoter, which contains two conserved CREB3L2-binding sites but lacks Xbp1 motifs, was specifically activated by CREB3L2, but not by Xbp1s. This specificity was confirmed through transient transfection-based reporter assays in 293T cells, EMSAs, and in bEnd.3 cells stably integrated with a *Fut7* promoter-driven reporter. Activation of CREB3L2 by Brefeldin A (BFA)[55], which induces ER-Golgi fusion and CREB3L2 processing, robustly upregulated reporter activity in bEnd3 cells. By contrast, the reporter activity was suppressed by either S1P protease inhibitor (PF-429242) or S2P protease inhibitor (nelfinavir)[56,57], which block CREB3L2 activation, but was unaffected by the IRE1α inhibitor STF-083010 (Fig. 3D–F)[58].

Finally, Xbp1s and CREB3L2 cooperatively enhanced transcription of reporter constructs driven by the *Pgm3*, *Nans*, and *C1galt1* enhancer-promoter elements (Fig. 3G). Together, these data demonstrate that Xbp1s and CREB3L2 directly regulate gene expression via conserved regulatory motifs in key genes required for precursor and glycan biosynthesis, extending their role beyond ER-localized targets.

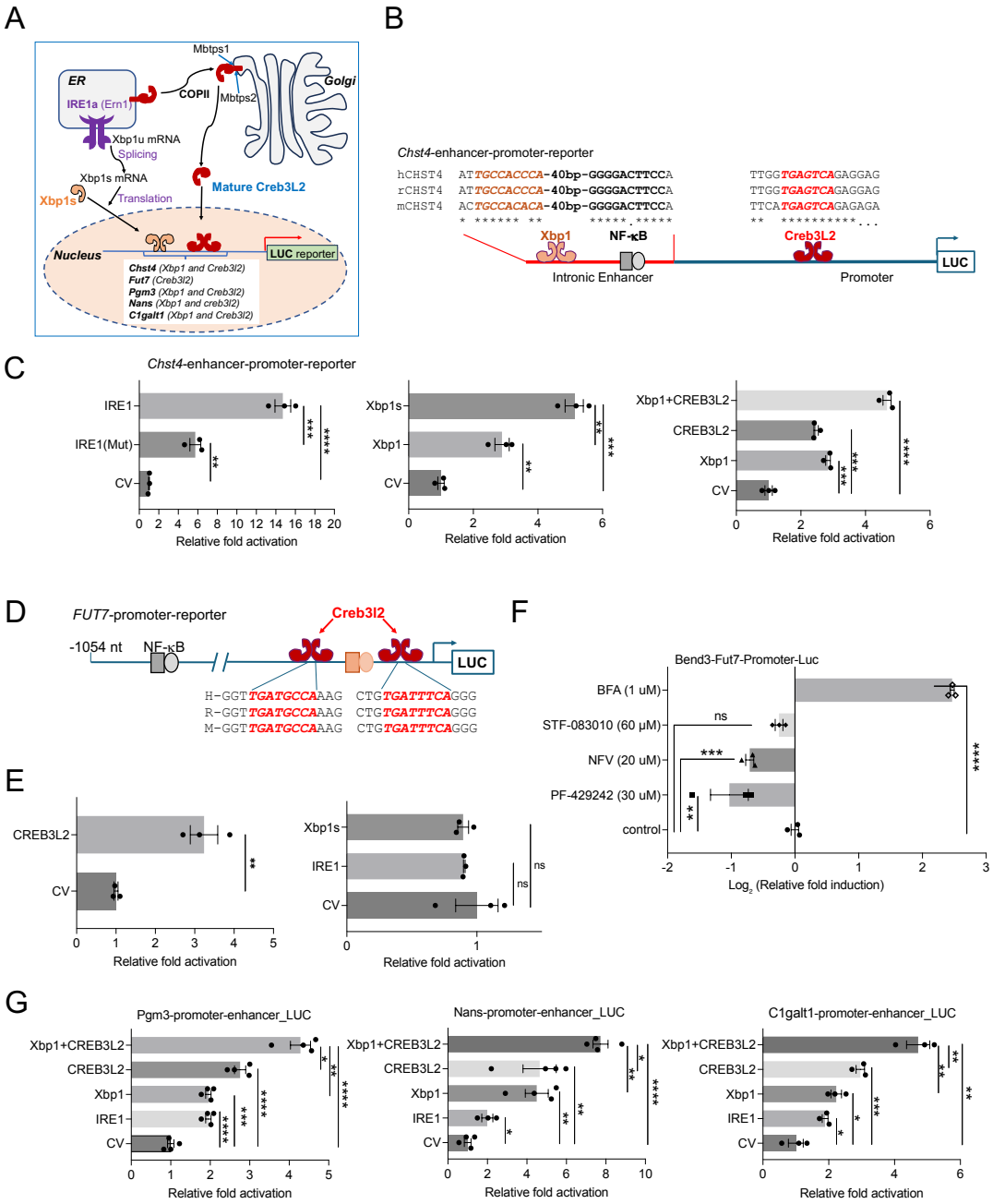

Fig.3. Xbp1 and CREB3L2 Transcriptionally Activate PNAd Biosynthetic Genes.

A. A schematic of XBP1 and CREB3L2 activation and their subsequent transactivation of genes functioning across the Golgi and cytosol for PNAd synthesis.

B. Evolutionarily conserved XBP1- and CREB3L2- binding motifs on the *Chst4* enhancer-promoter-driven luciferase reporter.

C. IRE1, Xbp1s, and CREB3L2 coordinately enhance luciferase reporter activity driven by the *Chst4* enhancer-promoter in 293T cells. Fold inductions relative to the control vector (CV) are shown.

D. Evolutionarily conserved CREB3L2-binding motifs on the *Fut7* promoter-driven reporter.

E. CREB3L2, but not IRE1 or Xbp1s, enhances *Fut7* promoter-driven reporter activity in 293T cells. Fold inductions relative to the CV are shown.

F. In bEnd.3 cells stably expressing *Fut7* promoter-driven reporter, CREB3L2 activation by BFA upregulates the reporter activity, whereas S1P/S2P inhibitors (PF-429242/NFV) suppress the reporter activation, and IRE1α inhibition (STF-083010) has no effect.

G. Overexpression of Xbp1s and/ or active CREB3L2 enhances luciferase activity driven by *Pgm3*, *Nans*, and *C1galt1* promoter-enhancers in 293T cells. For C, D, and G, fold inductions are shown relative to the CV; For F, $\log_2$ (fold induction relative to vehicle) is shown. Values represent the mean ± SEM of three independent experiments. *: p value < 0.05; **: p value < 0.01; ***: p value < 0.001; ****: p value < 0.0001. Two-tailed t-test, unpaired.

Pharmacological Inhibition of Xbp1 or CREB3L2 Flattens HEVs, Reduces PNAd Expression, and Impairs Lymphocyte Homing

To test the role of IRE1α–Xbp1 and CREB3L2 signaling in maintaining HEV morphology and function *in vivo*, we pharmacologically inhibited each pathway in wild-type C57BL/6 mice. Mice were treated with either STF083010, a selective inhibitor of IRE1α RNase activity[58], or PF-429242, an S1P protease inhibitor that blocks CREB3L2 activation[59].

Following treatment, peripheral lymph nodes (PLNs) were analyzed by whole-mount immunofluorescence (IF) using anti-CD31 to label vasculature and MECA-79 to detect the extended core 1 epitope of PNAd[60,61]. PLNs from STF083010- and PF-429242–treated mice displayed marked structural abnormalities, including reduced node size, flattened and elongated HEV walls, and diminished vascular branching (Fig. 4A; Suppl. Fig. 5A). PNAd expression was significantly reduced, as quantified by PNAd$^+$ HEV surface area relative to total CD31$^+$ vasculature (Fig. 4B, G). These structural defects in HEV were accompanied by a substantial decrease in total lymphocyte numbers within the PLNs (Fig. 4C, H).

To test whether lymphocyte homing was impaired, we next assessed homing efficiency using adoptive transfer assays. Splenocytes were injected i.v. and quantified in recipient LNs 2 hours later. Lymphocyte recruitment to PLNs and mesenteric lymph nodes(MLNs) were significantly reduced in both inhibitor-treated groups, whereas homing to Peyer's patches (PPs)—where HEVs are MAdCAM-1$^+$/PNAd$^-$[62]—and to the spleen remained largely unaffected (Fig. 4D, I; Suppl. Fig. 5B, D). Consistent with the role of HEV in determining endogenous as well as injected lymphocyte accumulation, the donor-to-recipient lymphocyte ratios in LN were comparable between treatment and control groups (Suppl. Fig. 5C, E).

We also examined the effects of IRE1α–Xbp1 and CREB3L2 inhibitors on short-term lymphocyte arrest and diapedesis across HEV[63]. CellTracker-labeled splenocytes were intravenously transferred into treated and control mice, and their localization (in HEV and in the surrounding parenchyma) was assessed 30 minutes later by confocal microscopy. LNs from both STF083010- and PF-429242–treated mice showed marked reductions in HEV-bound and extravasated lymphocytes (Fig. 4E, F for STF083010; Fig. 4J, Suppl Fig. 5F for PF-429242), and a significant decrease in the ratio of extravasated to HEV bound cells. These data indicate that pharmacologic inhibition of IRE1α–Xbp1 or Creb3L2 pathways results in diminished PNAd expression, HEV "highness", impaired lymphocyte-HEV interactions and reduced transmigration efficiency.

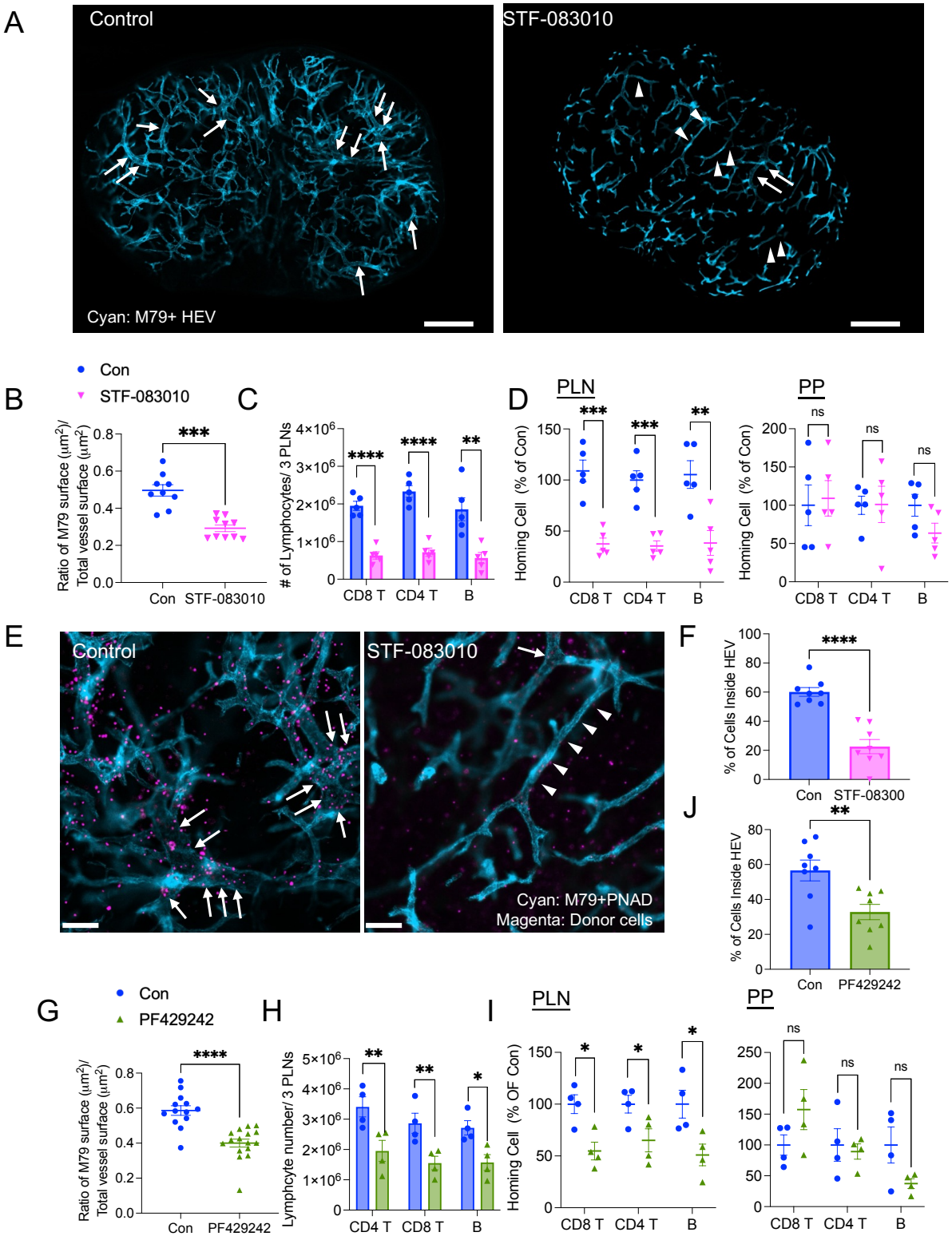
A
Control
STF-083010
Cyan: M79+ HEV
B
Con
STF-083010
Ratio of M79 surface (μm²)/ Total vessel surface (μm²)
Con
STF-083010
C
# of Lymphocytes/ 3 PLNs
CD8 T
CD4 T
B
D
PLN
PP
Homing Cell (% of Con)
CD8 T
CD4 T
B
E
Control
STF-083010
Cyan: M79+PNAD
Magenta: Donor cells
F
% of Cells Inside HEV
Con
STF-08300
J
% of Cells Inside HEV
Con
PF429242
G
Con
PF429242
Ratio of M79 surface (μm²)/ Total vessel surface (μm²)
Con
PF429242
H
Lymphcyte number/ 3 PLNs
CD4 T
CD8 T
B
I
PLN
PP
Homing Cell (% OF Con)
CD8 T
CD4 T
B

Fig. 4. Pharmacological Inhibition of Xbp1 or CREB3L2 Flattens HEVs, Reduces PNAd Expression, and Impairs Lymphocyte Homing

A. Representative whole-mount immunofluorescence (IF) images of PLNs from STF-083010–treated and control mice. Mice were injected intravenously (i.v.) with antibodies to label PNAd (MECA-79, cyan) and CD31 (not shown). Arrows denote thick HEV segments; arrowheads indicate thin, elongated HEVs. Scale bar: 500 µm.

B. Quantification of PNAd$^+$ (MECA-79$^+$) HEV surface area relative to total CD31$^+$ vasculature by Imaris analysis. Data represent 1 field per PLN, 2–4 fields per mouse from 3 independent experiments (1 control and 1 STF-083010–treated mouse per experiment).

C. Lymphocytes counts from 3 pooled PLNs (Inguinal, Axillary, and Branchial PLN) per STF-083010-treated and control mouse.

D. Flow cytometry analysis of donor lymphocyte homing to PLNs and PPs 2 hours post-transfer in control vs. STF-083010–treated mice, expressed as percentage of control group mean localization ratio. C–D: Results are pooled data (mean ± SEM) from n = 5 mice per group.

E. Representative IF images of PLNs 30 minutes after short-term diapedesis assay. Donor lymphocytes (CFSE-labeled, magenta), PNAd (cyan). Arrows highlight thick HEV segments containing donor cells; arrowheads denote thin, elongated HEVs. Scale bar: 100 µm.

F. Percentage of donor cells localized inside MECA-79$^+$ HEVs, quantified by Imaris. Data collected from 1 field/PLN, 2–3 fields/mouse across 3 independent experiments (1 control and 1 STF-083010–treated mouse per experiment).

G. Quantification of MECA-79$^+$ HEV surface area relative to CD31$^+$ vasculature in control and PF-429242–treated mice. Data collected from 2–6 fields/mouse across 3 independent experiments (1 control and 1 treated mouse per experiment).

H. Total lymphocyte counts from pooled 3 PLNs (inguinal, axillary, brachial) in PF-429242–treated and control mice.

I. Flow cytometry analysis of donor lymphocyte homing to PLNs and PPs in PF-429242–treated vs. control mice, assessed 2 hours post-transfer and expressed as percentage of WT group mean. H-I: Results are pooled data (mean ± SEM) of n=4 mice per group.

J. Imaris analysis of short-term diapedesis assay in PF-429242–treated vs. control mice. Percentage of donor cells inside MECA-79$^+$ HEVs calculated from 2–3 fields/mouse across 3 independent experiments (1 control and 1 treated mouse per experiment).

All data are shown as mean ± SEM. *: p value < 0.05; **: p value < 0.01; ***: p value < 0.001; ****: p value < 0.0001. Two-tailed unpaired t-test (B–D, F–J).

Endothelial Xbp1 Preserves HEV morphology, Supports Lymphocyte Recruitment, and Sustains Inflammatory Immune Responses

To investigate the endothelial cell (EC)-specific role of IRE1α-Xbp1 signaling in maintaining HEV structure and function, we generated conditional EC-specific Xbp1 knockout (iEC_Xbp1-/-) mice by crossing a tamoxifen-inducible Cre system Cdh5CreERT2[64] with Xbp1tm2Glm fl/fl[65]. Tamoxifen treated Cdh5CreERT2 negative littermates served as WT controls. All groups were evaluated 4–10 weeks after tamoxifen injection.

Deletion of Xbp1 in ECs resulted in a significant reduction in LN size (Fig. 5A, left; Suppl. Fig. 6A). Whole-mount IF imaging revealed diminished PNAd expression (Fig. 5B), reduced HEV branching (Fig. 5A, right), and characteristic HEV flattening in Xbp1-deficient mice (Fig. 5A-C; Suppl. Fig. 6B).

Lymphocyte recruitment was severely impaired in iEC_Xbp1-/-mice. Total lymphocyte numbers in peripheral LNs were reduced by ~65% compared to WT controls (Suppl. Fig. 6C), and short-term (2 hours) homing assays showed ~50% reduction in lymphocyte accumulation in both PLNs and MLNs, while Peyer's patches (PPs) and spleens were unaffected (Fig. 5D; Suppl. Fig. 6D). Donor-to-recipient lymphocyte ratios remained comparable between groups (Suppl. Fig. 6E), confirming that reduced recruitment was not due to altered donor cell viability. *In vivo* diapedesis assays further revealed a ~60% decrease in lymphocyte adhesion to HEVs and an ~85% reduction in extravascular to HEV-associated lymphocyte ratios in Xbp1-deficient LNs (Fig. 5E), confirming compromised lymphocyte–HEV interaction and transmigration.

To assess whether EC-specific Xbp1 depletion impacts immune function, we evaluated contact hypersensitivity responses in iEC_Xbp1-/- and WT littermate mice following sensitization and challenge with the hapten DNFB (2,4-dinitrofluorobenzene)[66]. Xbp1

deletion significantly attenuated ear swelling and leukocyte infiltration (Fig. 5F–G). $CD4^+$ T cells, including memory subsets ($CD4^+$CD44^highCD45RB^low, were markedly reduced in the draining lymph nodes (auricular and inguinal) and inflamed ear tissue of knockout mice compared to controls (Fig. 5H–I). MECA-79^+ HEV-like vessels were absent from DNFB-inflamed ear skin in both genotypes (data not shown). These findings support a critical role for endothelial Xbp1 in induction of inflammatory immune responses within draining lymph nodes, although we cannot exclude the possibility that Xbp1 also influences inflamed venular structures in extralymphoid tissues.

Together, these results demonstrate that endothelial Xbp1 is required to maintain the specialized “high” endothelial phenotype, promote PNAd expression, support HEV integrity, and enable effective lymphocyte recruitment during both homeostatic and inflammatory immune responses.

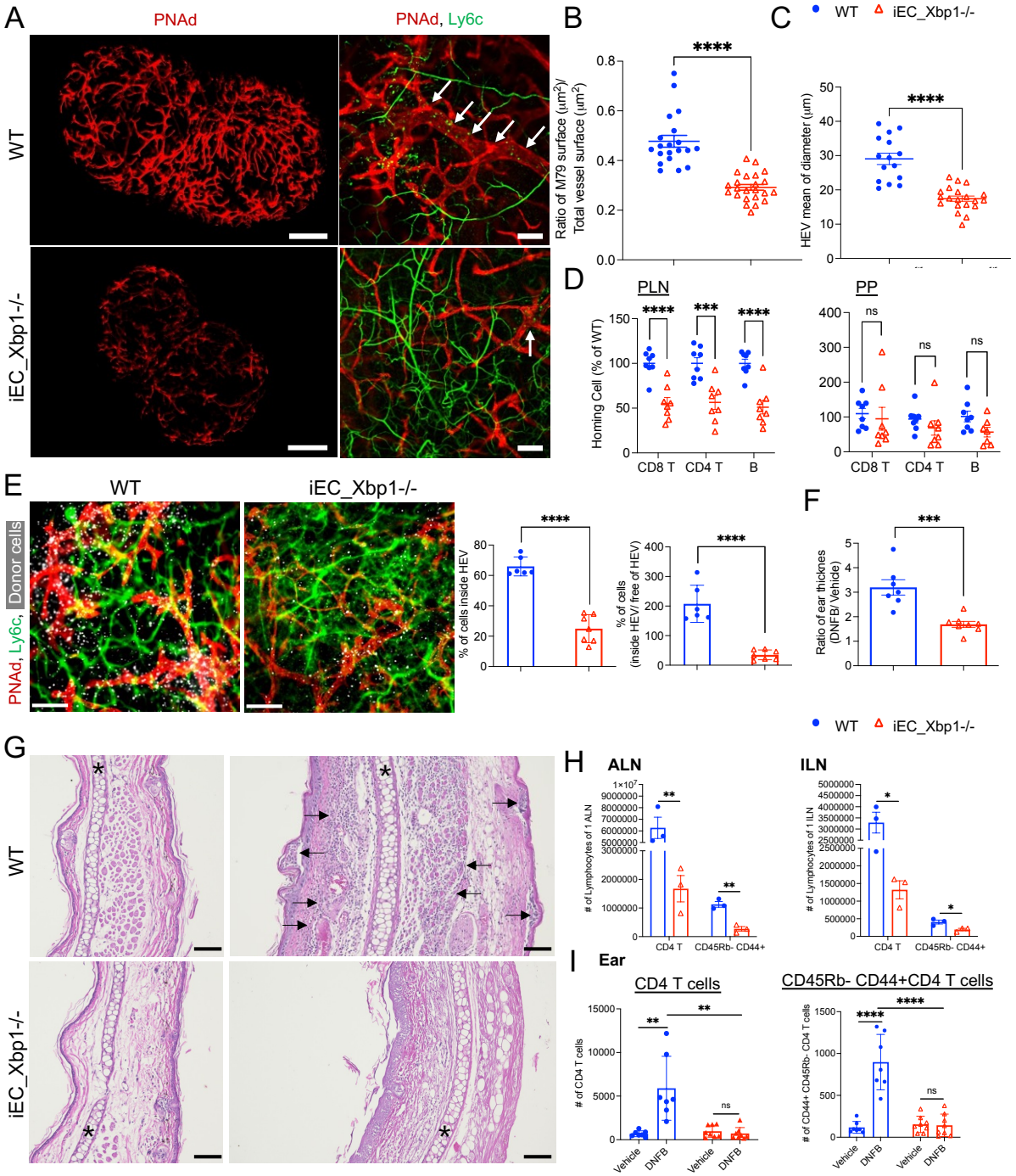

Fig.5. EC-specific Depletion of Xbp1 Flattens HEVs, Reduces PNAd Expression, Impairs Lymphocyte Trafficking, and Dampens Inflammatory Immune Responses.

A. Representative vascular IF images of PLN from WT control and iEC_Xbp1-/-mice. Mice were intravenously injected with antibodies against PNAd (MECA-79, red), Ly6C (green), and CD31 (not shown). Representative images from five independent experiments, each with one mouse per group per experiment. Arrows show thick HEV segments, arrow heads indicate elongated thin HEV. Scale bars: 100 μm;

B. Quantification of PNAd⁺ HEV surface area relative to CD31⁺ vasculature using Imaris.

C. Measurement of HEV diameter. Results are presented as the mean of 14-35 measurements per 10X field (~4 mm2/field). (B-C): Data are shown as mean ± SEM from 2-3 fields per PLN, 1-2 PLN per mouse, n=5 per group.

D. Donor lymphocyte localization in PLNs and Peyer's patches (PPs) 2 hours post-transfer in control and iEC_Xbp1-/- mice. Results are shown as a percentage of the mean localization ratio to the WT group (mean ± SEM of with 8 mice per group).

E. Left: Visualization of CFSE-labeled donor lymphocytes (white) within PLNs from control and Xbp1-deficient mice, 30 minutes post transfer (i.v.). Vessles were stained with anti-PNAd (red) and anti-Ly6C (green). Arrows show thick HEV segments containing donor cells, stars mark free cells in capillaries; Scale bar: 100 µm. Right: Quantification of donor cell localization within PNAd$^+$ HEVs and calculation of intra- vs. extravascular lymphocyte ratios using Imaris. Data are presented as mean ± SEM from 1–2 lymph nodes per mouse, n=4 mice per group.
F-I: Attenuation of contact hypersensitivity responses in iEC_Xbp1-/-mice. **F.** Ear swelling ratio (DNFB/vehicle) measured 24 hours after challenge.
G. H&E staining of ear tissue; stars indicate cartilage, arrowheads denote infiltrating leukocytes. Scale bar: 100 µm.
H-I. Flow cytometery analysis of total and memory CD4$^+$ T cells in auricular LN (ALN, H left), inguinal LN (ILN, H right) and inflamed ears (I). H: WT: n = 3; iEC_Xbp1-/-: n = 3. I WT: n = 7; iEC_Xbp1-/-: n = 8
Data are shown as mean ± SEM. Statistical analysis was performed using two-tailed unpaired t-tests. *: p value < 0.05; **: p value < 0.01; ***: p value < 0.001; ****: p value < 0.0001.

Xbp1 intrinsically controls Inter-Organelle Metabolic Coordination, Organelle Integrity, and PNAd Biosynthesis in HECs

To define how Xbp1 sustains PNAd biosynthesis and organelle function *in vivo*, we performed single-cell RNA sequencing (scRNA-seq) of Xbp1-deficient HEC (from iEC Xbp1-deficient mice) vs WT HEC. Xbp1-deficient HECs exhibited broad downregulation of genes essential for PNAd biosynthesis, including key enzymes of nucleotide sugar synthesis pathways (e.g., Gale, Gpi1, Pgm3, Uap1, Nans, Cmas), nucleotide sugar transporters (Slc35a1, Slc35b3), and glycosyltransferases (Galnt12, C1galt1, C1galt1c1, Fut7, Chst4) (Fig. 6A). Expression of genes critical for maintaining secretory organelle function was also reduced, including Ssr1 (ER-targeted protein translation), Bet1 (COPII trafficking), Derl1, Derl2 (ER-associated degradation), Mbtps1, Mbtps2 (CREB3L2 proteolytic activation), and Golph3 (COPI adaptor for glycosyltransferase positioning)[67]. These transcriptional changes are consistent with our motif analysis (Fig. 2D) and reporter assays (Fig. 3), supporting direct regulation of these pathways by Xbp1. Canonical markers of pan-endothelial, venous, and capillary identity remained intact, indicating that Xbp1 specifically regulates the metabolic and structural programs required for the high endothelial specialization. Ern1 (IRE1α) expression was paradoxically upregulated in Xbp1-deficient HECs, a response previously associated with pro-apoptotic signaling and cell stress in other Xbp1 knockout models[22].

To assess the effects of EC-specific Xbp1 deficiency on organelle architecture and cellular integrity in HECs, we examined peripheral LN vasculature by transmission electron microscopy (TEM). Xbp1-deficient HECs displayed profound ultrastructural abnormalities, including cellular flattening, distorted ER membranes with ribosome dissociation, and prominent autophagic vacuoles containing engulfed mitochondria (Fig. 6B). Additional features included early-stage mitophagy, degraded mitochondrial remnants, disrupted polysomes, osmiophilic deposits, and endothelial stress markers such as platelet adhesion (Suppl. Fig. 7B–C). These morphological changes indicate severe organelle stress and compromised biosynthetic capacity. Together, these results demonstrate that endothelial Xbp1 is essential for coordinating metabolic gene expression, preserving organelle architecture, and sustaining PNAd biosynthesis and HEC survival.

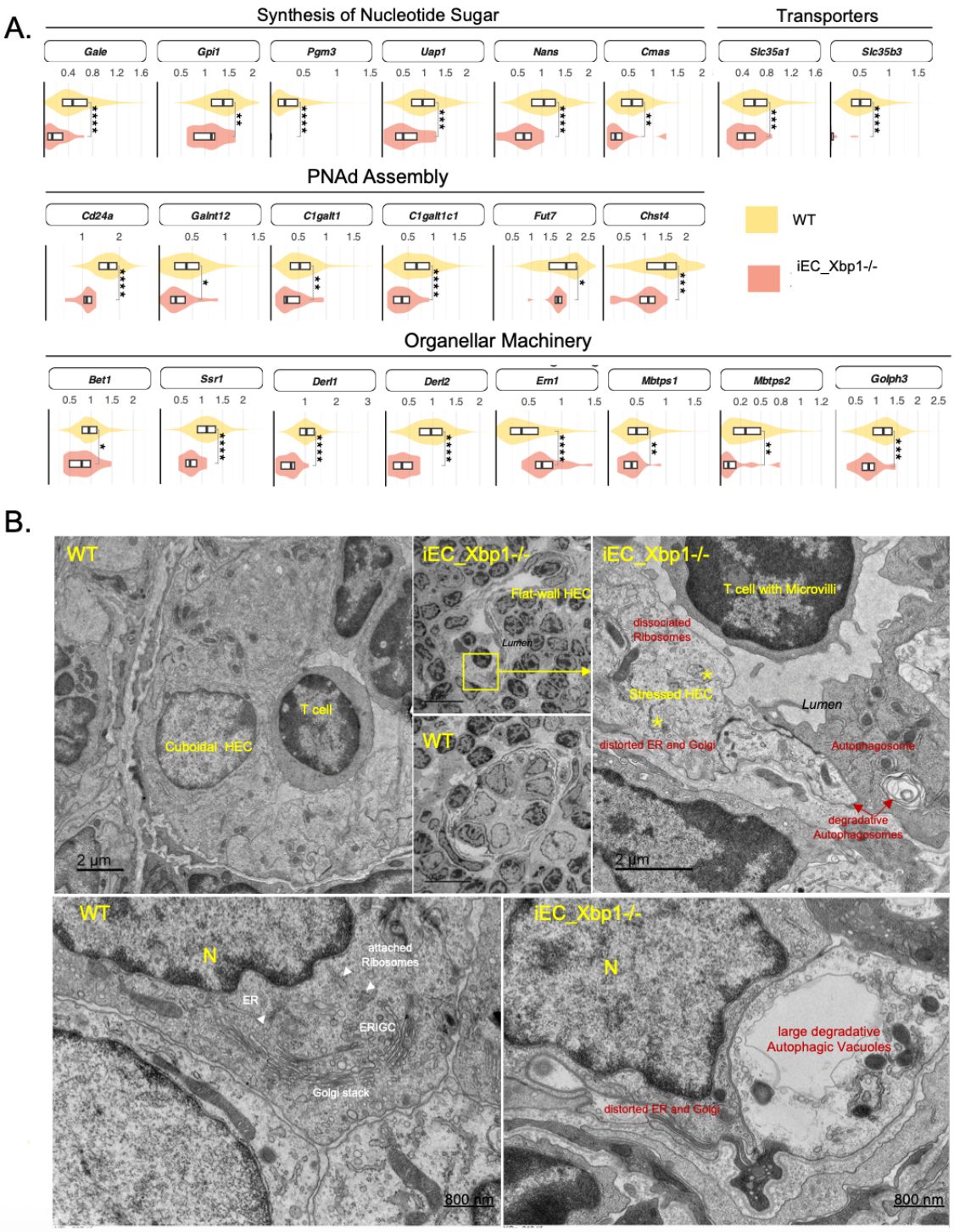

Fig. 6. Endothelial Xbp1 Is Required For Inter-Organelle Metabolic Coordination, Organelle Integrity, and PNAd Biosynthesis in "High" HECs.

A. scRNA-seq of HECs from WT and iEC_Xbp1-/- mice reveals broad downregulation of genes involved in nucleotide sugar biosynthesis, nucleotide sugar transport, PNAd Assembly, and organellar machinery components as indicated. Violin plots show normalized expression values in Xbp1-deficient versus WT HECs. Data are presented as mean ± SEM, n = 2 mice per group. Statistical significance determined by unpaired two-tailed t-test: **: p value < 0.05; **: p value < 0.01; ***: p value < 0.001; ****: p value < 0.0001.*

B. TEM of peripheral LNs from WT and iEC_Xbp1-/-mice reveals multiple subcellular organelle defects in Xbp1-deficient HECs. N, nucleus; M, mitochondria; ER, endoplasmic reticulum; AP, autophagosome. Scale bars: 2 µm, 10 µm, and 800 nm. Images are representative of n = 3 mice per group.

Xbp1 Is Required for HEV Expansion and Ectopic Induction During Immune Activation

During immune activation, high endothelial venules (HEVs) undergo dynamic expansion through immune-driven angiogenesis, facilitating enhanced lymphocyte recruitment and enlargement of draining lymph nodes (LNs)[68,69]. To assess whether endothelial Xbp1 is required for this process, we used a cutaneous inflammation model induced by topical application of 5% oxazolone (OXA)[70]. Four days after treatment, LNs from wild-type (WT) mice exhibited robust HEV proliferation and branching (Fig. 7A). In contrast, endothelial-specific Xbp1-deficient mice displayed markedly thinner, sparsely branched PNAd$^+$ vessels with reduced PNAd expression (Fig. 7A–B), demonstrating that Xbp1 is critical for HEV remodeling and expansion during inflammatory angiogenesis.

We next examined the role of Xbp1 in the atypical lymphoid structures of omental milky spots (MSs), immune aggregates within the peritoneal cavity that rely on induced PNAd$^+$ vessels for lymphocyte recruitment and tissue organization[18,71]. Previous studies show that MS-associated HEVs are rapidly induced by microbial stimuli such as lipopolysaccharide (LPS) and that loss of HEV formation disrupts MS architecture[72,73]. Following intraperitoneal LPS administration, WT mice exhibited robust and rapid induction of PNAd$^+$ vessels within MSs following two intraperitoneal LPS injections over 72 hours, whereas this response was significantly attenuated in Xbp1-deficient mice (Fig. 7C–D). These results identify Xbp1 as a key regulator of ectopic HEV formation in during immune activation.

Given that HEV-like vessels also emerge de novo in sites of chronic inflammation[18,74]and are implicated in various human inflammatory diseases and tumor microenvironments[8,75-78], we next tested whether Xbp1 is required for HEV-like vessel induction in peripheral inflamed tissues. Using an oxazolone-induced model of atopic dermatitis[70], we applied oxazolone bilaterally to the ears of tamoxifen-treated iEC_Xbp1-/-and WT mice and analyzed vascular remodeling ten days later. WT mice developed prominent PNAd$^+$ HEV-like vessels in inflamed ear skin, whereas Xbp1-deficient mice showed markedly reduced induction of these vessels (Fig. 7E–F).

Together, these findings establish Xbp1 as a critical regulator of PNAd$^+$ HEV expansion and ectopic HEV formation across lymph nodes, atypical lymphoid tissues, and peripheral inflamed organs. By enabling the molecular specialization of HEV, Xbp1 shapes local immune architecture and modulates tissue-specific immune responses during inflammation.

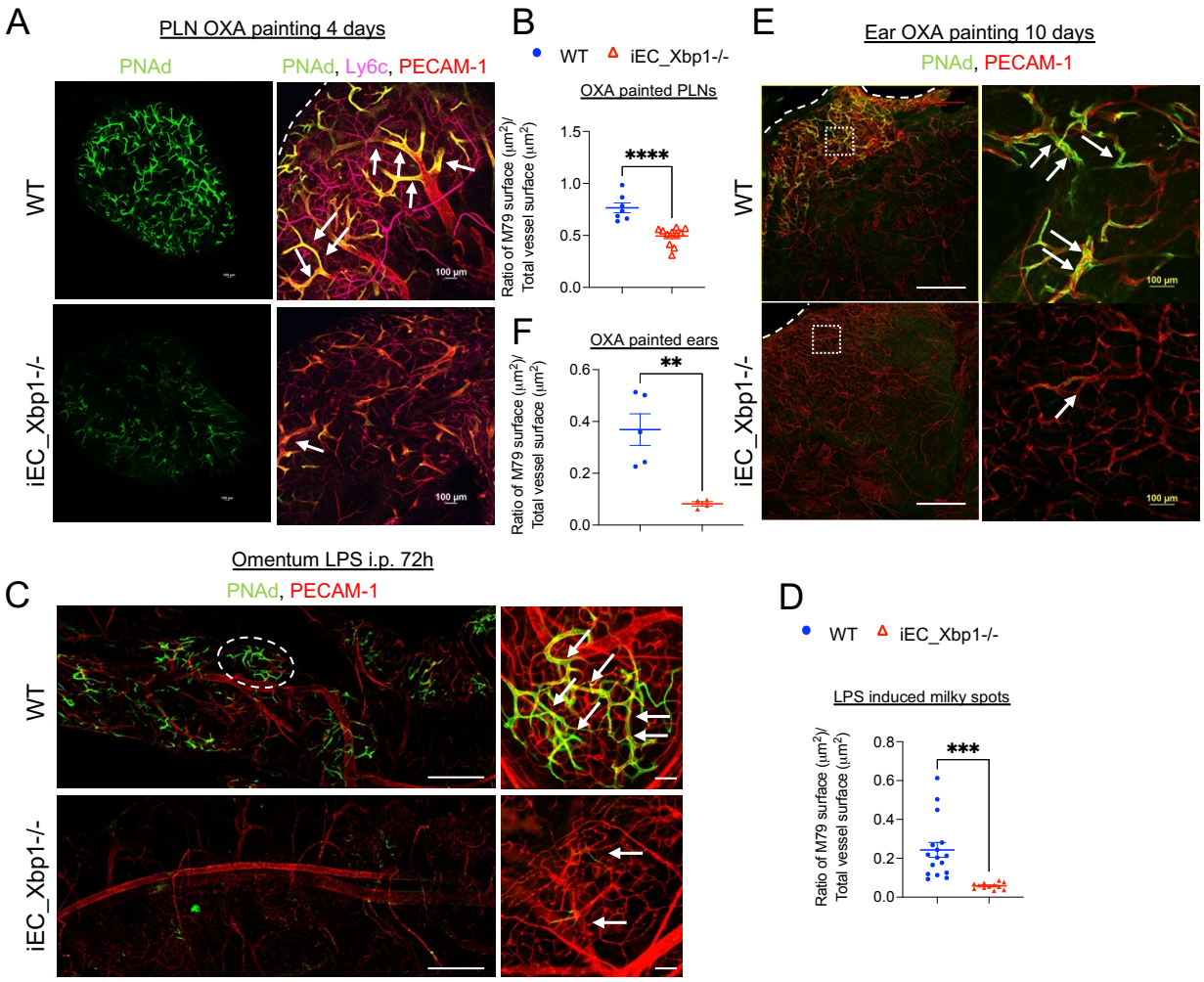

Fig. 7. Xbp1 is required for PNAd⁺ HEV expansion and ectopic HEV-like vessel induction during immune activation. (268)

A. Representative whole-mount IF images of PLNs from WT and iEC_Xbp1-/- mice, four days after OXA-induced cutaneous inflammation. Intravenous labeling with antibodies against PNAd (MECA-79, green), Ly6C (pink), and CD31 (red) highlights HEV morphology and surface markers. Dashed lines indicate LN boundaries; arrows denote PNAd extension along HEV segments. Scale bars, 100 µm.

B. Quantification of PNAd⁺ HEV surface area relative to total CD31⁺ vasculature, measured using Imaris analysis. Data represent mean ± SEM from 2 fields per lymph node; 1–2 lymph nodes per mouse: WT (n = 3), iEC_Xbp1-/- (n = 3).

C. Left: Whole-mount omental staining of WT and iEC_Xbp1-/- mice following two intraperitoneal LPS injections over 72 hours. Right: Representative milky spots showing induced PNAd⁺ vessels (green) within CD31⁺ vasculature (red). Arrows highlight induction of PNAd+ HEVs. Scale bars, 100 µm.

D. Quantification of the PNAd⁺/CD31⁺ vessel area ratio within milky spots, based on 10× fields (~4 mm²/field), analyzed using Imaris. Data represent mean ± SEM from 3-4 fields per mouse; n = 4 mice per group.

E. Whole-mount IF of ear vasculature ten days after bilateral OXA application. Left: overview of entire ear; right: higher-magnification views of inflamed skin showing PNAd⁺ vessels (green) and CD31⁺ endothelium (red). Dashed lines mark ear boundaries; arrows indicate PNAd⁺ HEV-like vessels. Scale bars, 100 µm.

F. Quantification of PNAd⁺ vessel area in inflamed ear skin, analyzed using Imaris. Data represent mean ± SEM from 1 field per ear; WT (n = 5), iEC_Xbp1-/- (n = 3). (B, D and F) Statistical analysis performed using paired two-tailed t-tests: *: p value < 0.05; **: p value < 0.01; ***: p value < 0.001; ****: p value < 0.0001.

Discussion

Understanding how cells coordinate metabolic transformations to establish their morphology, function, and identity remains a central challenge in cell biology, physiology, and disease[2,5]. Secretory cells, in particular, must scale biosynthetic capacity with structural specialization to meet intense functional demands. Here, we define CREB3L1/2 and IRE1α-XBP1-driven transcriptional networks as central regulators of this process in high endothelial cells (HECs) and intestinal goblet cells (GCs)—lineages programmed for mass production of structurally complex, sulfated mucin-type O-glycans for lymphocyte homing and mucosal barrier defense, respectively[8,79]. These circuits orchestrate the expression of nutrient transporters, metabolic enzymes, endomembrane transporters, glycosyltransferases, organelle protein machineries, and cargo trafficking components, coupling metabolic flux to organelle function to enable specialized and amplified production of sulfated mucins.

A central feature of these transcriptional programs is their ability to integrate precursor biosynthesis with the scaling of secretory organelles. PNAd biosynthesis, as an example, requires sustained production of nucleotide sugar donors (including UDP-GalNAc, UDP-GlcNAc, GDP-Fuc, CMP-Neu5Ac), sulfate donors (PAPS), and the coordinated deployment of glycosyltransferases and sulfotransferases within the Golgi apparatus. Our data show that these metabolic pathways do not operate in isolation but are tightly coupled to ER and Golgi expansion, protein folding capacity, and cargo trafficking systems. This integration ensures the efficient assembly of complex glycan structures, including the 6-sulfo sialyl Lewis X (6-sulfo sLe^X) moieties that decorate PNAd mucins in HECs. Such coupling between metabolic flux and organelle architecture provides a mechanistic framework for how secretory cells achieve both structural and biosynthetic specialization.

Our analysis positions IRE1α-XBP1 and CREB3L1/2 as direct regulators of these integrated biosynthetic and organellar programs. Both factors engage conserved binding motifs within non-coding regulatory elements across genes involved in glycan biosynthesis, cargo trafficking, organelle scaling, and precursor transport. Activation of XBP1 via IRE1α-mediated splicing and CREB3L1/2 through regulated intramembrane proteolysis allows these networks to respond dynamically to secretory demand and ER stress. The recurrent co-occurrence of XBP1 and CREB3L1/2 binding motifs within evolutionarily conserved regions suggests that these transcription factors can function cooperatively as well as independently, and we confirm cooperative XBP1/CREB3L2 control of gene expression from the promoter/enhancer regions of genes involved in PNAd synthesis using *in vitro* reporter assays. Through this dual control, these pathways integrate ER stress-responsive signaling with lineage-specific transcriptional programming to reinforce glycosylation output and organelle scaling.

Beyond steady-state biosynthesis, these regulatory circuits enable adaptive remodeling of secretory capacity in response to immune challenge and inflammatory stress. In HECs, XBP1 and CREB3L2 sustain the cuboidal endothelial morphology, ER and Golgi

expansion, and PNAd expression required for efficient lymphocyte recruitment. Pharmacological inhibition or genetic disruption of these pathways flattens HEV morphology, reduces PNAd production, and impairs lymphocyte homing, highlighting their essential role in vascular specialization. Notably, these same transcriptional regulators govern ectopic HEV induction in chronic inflammation, where they support vascular remodeling and lymphocyte recruitment into non-lymphoid tissues. A parallel mechanism appears to operate in goblet cells, where XBP1 and CREB3L1/2 are positioned to maintain sulfated mucin biosynthesis and organelle capacity, ensuring effective mucosal barrier function[44,80,81]. Together, these findings suggest that coupling metabolic input to organelle architecture through shared transcriptional networks is a conserved strategy for sustaining secretory output across distinct tissue contexts.

More broadly, our work defines a generalizable regulatory logic by which secretory cells integrate metabolic flux with organellar function and architecture to achieve glycosylation-dependent specialization. While this study focuses on HECs and GCs, the engagement of IRE1α-XBP1 and CREB3 family factors across diverse secretory lineages—including plasma cells, hepatocytes, and pancreatic β-cells—raises the possibility that similar programs operate widely within mucin-producing epithelia and other secretory systems. Strikingly, a homologous mechanism may operate in *Drosophila*, where CrebA—the sole CREB3 family member— and Xbp1 together regulate secretory machinery in the salivary gland , suggesting the deep evolutionary conservation of this regulatory architecture[82].This conserved network may represent a core solution for scaling biosynthetic output under both homeostatic and stress-adaptive conditions. Further investigation into how these transcriptional circuits interface with lineage-specific and signal-induced programs may yield insights into the modulation of secretory capacity in health and disease. Additionally, these pathways may provide strategic entry points for therapeutic glycoengineering or for manipulating vascular and epithelial remodeling in inflammation-associated conditions.

Limitations and Future Directions

While this study establishes IRE1α-XBP1 and CREB3L1/2 as master regulators linking metabolism to organelle architecture in HECs and GCs, it has limitations. Our conclusions are based on transcriptional regulation inferred from single-cell transcriptomics, motif analysis, promotor/enhancer function in reporter assays, and genetic perturbation, but direct *in vivo* validation of cis-regulatory interactions at endogenous loci remains incomplete. The extent of cooperativity between XBP1 and CREB3L1/2, and how these factors interface with additional lineage-defining regulators across different tissue contexts, require further investigation. For instance, we identified conserved XBP1 and CREB3L1/2 motifs within immune-responsive genes such as Ltbr, Relb, and Nfkb2, as well as within GC lineage-specific regulators including Spdef and Klf4 (Data S1), suggesting a point of intersection between lymphotoxin-driven noncanonical NF-κB signaling and intrinsic secretory programming. It also remains unclear whether similar transcriptional networks operate broadly across other secretory lineages, such as plasma cells or hepatocytes. Finally, the degree to which environmental cues—including cytokines, metabolic inputs, and ER stress—modulate these pathways to fine-tune

secretory output has yet to be fully defined. Addressing these limitations will refine the mechanistic insights generated here and their relevance for therapeutic modulation of glycosylation and vascular specialization.

Resource availability

Lead contact

For more information and resource requests, please contact Yuhan Bi (yub10@stanford.edu), who will collaborate with the Butcher Lab as needed.

Materials availability

Reagent resources are available upon request to the lead contact.

Code Availability

scRNA-seq analysis was performed using publically available software. Code for computing imputed expression values is available: https://github.com/kbrulois/magicBatch.

Data Availability

The authors declare that all data supporting the findings of this study are available within the article and its supplementary information files. Raw and processed scRNA-seq data generated in this study are available from the NCBI Gene Expression Omnibus repository under the accession number GSE296739. Source data are provided with this paper. De novo motif discovery on HEC-enriched genes are provided as a custom track in a UCSC Genome Browser session: https://genome.ucsc.edu/s/m.xiang/HEV_genes_conserved.

Acknowledgments

Supported by NIH grants R01 AI178113 and R01 AI047822, MERIT award I01 BX-002919 from the United States (U.S.) Department of Veterans Affairs, Biomedical Laboratory Research & Development Service, Grant 1903-03787 from The Leona M. & Harry B. Helmsley Charitable Trust to E.C.B. The Transmitted Electron Microcopy (TEM) study was supported, in apart, by NIH S10 Award Number 1S10OD028536-01, titled "OneView 4kX4k sCMOS camera for transmission electron microscopy applications" from the Office of Research Infrastructure Programs (ORIP). Y.B. and B.O. were supported by a Research Fellow Award of the Crohn's and Colitis Foundation of America (835171 and 574148). M.X. was supported by the Tobacco-Related Disease Research Program of University of California (T31FT1867). We thank John J. Perrino for TEM sample preparation and imaging. We thank L. Magalhaes for administrative support.

Author contributions

Y.B. conducted and oversaw experiments; K.B. performed single-cell RNA-seq analysis. M.X., Y.B., J.P. performed genomic analyses. A.A., R.B., B.O., M.K., T.D. and N.L.

performed experiments. G.R. helped with mouse colonies. R.S. advised TEM imaging and analysis. J.H.L. provided Xbp1tm2Glm fl/fl mice and scientific advice. Y.B. and J.P. conceived the study. Y.B., J.P. and E.C.B. wrote and K.B. edited the manuscript. E.C.B. and J.P. supervised the study.

Declaration of interests

The authors declare no competing interests.

Supplemental information

Data S1. Word file containing Phylogenetic DNA FootPrinting at Base-Resolution on Metabolic Flux for Sulfated Mucin-Type O-Glycans, Organelle Machinery as well as linage specific and immune responsive factors, related to Fig. 2D and Discussion.

Table S1. Multiple excel sheets of 2000 upregulated DEGs of each subsets of lymph node endothelium and colon epithelium, related to Fig. 1 & 2.

Table S2-4. Erichr TF analyses, related to Fig. 2.

Table S5. Construct information.

Supplemental Figures

Supplemental Fig.1

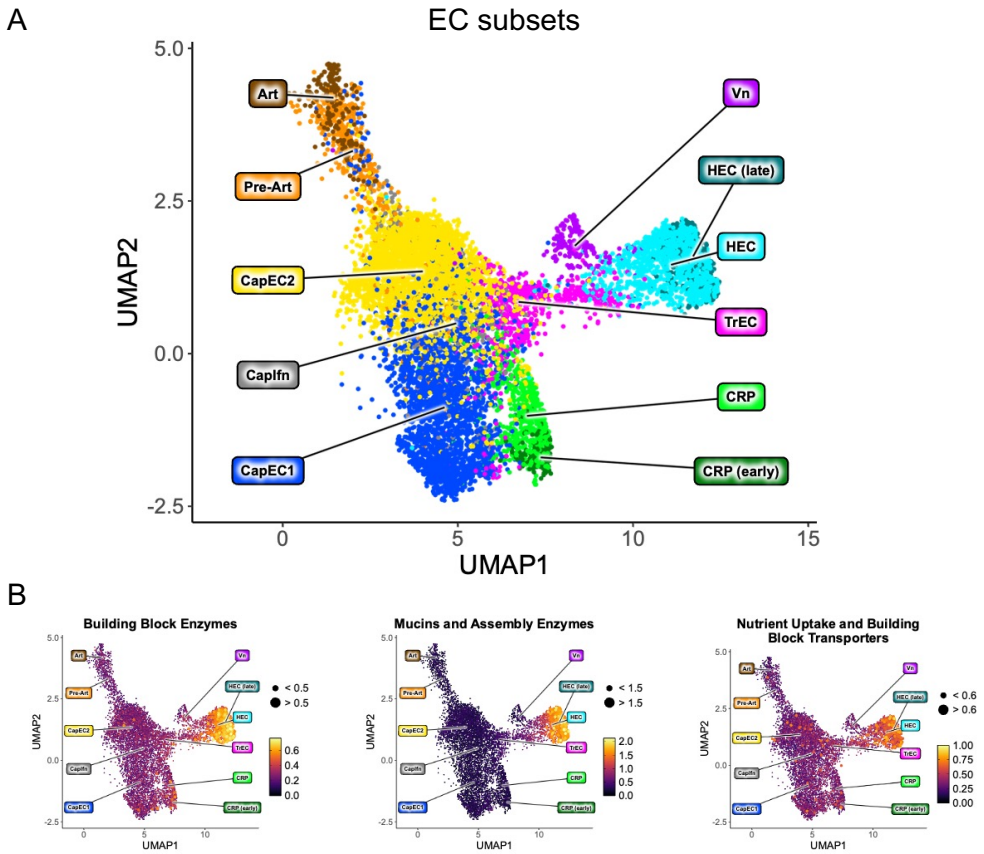

Suppl. Fig. 1. (linked to Figure 1)**. A.** UMAP projection of EC subsets from scRNA-seq profiling of murine peripheral lymph node ECs[26]. Cells are segregated by 11 subsets: arterial EC (pre-Art), high endothelial cells (HEC), non-HEC veins (Vn), and five capillary phenotype EC (CapEC1, CapEC2, capillary resident progenitors (CRP), transitional EC (TrEC), Interferon-stimulated gene-enriched CapEC (CapIfn). Results are represented on a color scale, with an asterisk (*) denoting the maximum value. **B**. The UMAP plots show the genes driving Building block enzymes (Left), Mucins and assembly enzymes (Middle), Nutrient update and building block transporters (Left), significantly enriched HECs compared to other EC subsets. Mean expression profiles of the genes used for these module scores are provided in C.

Supplemental Fig.2

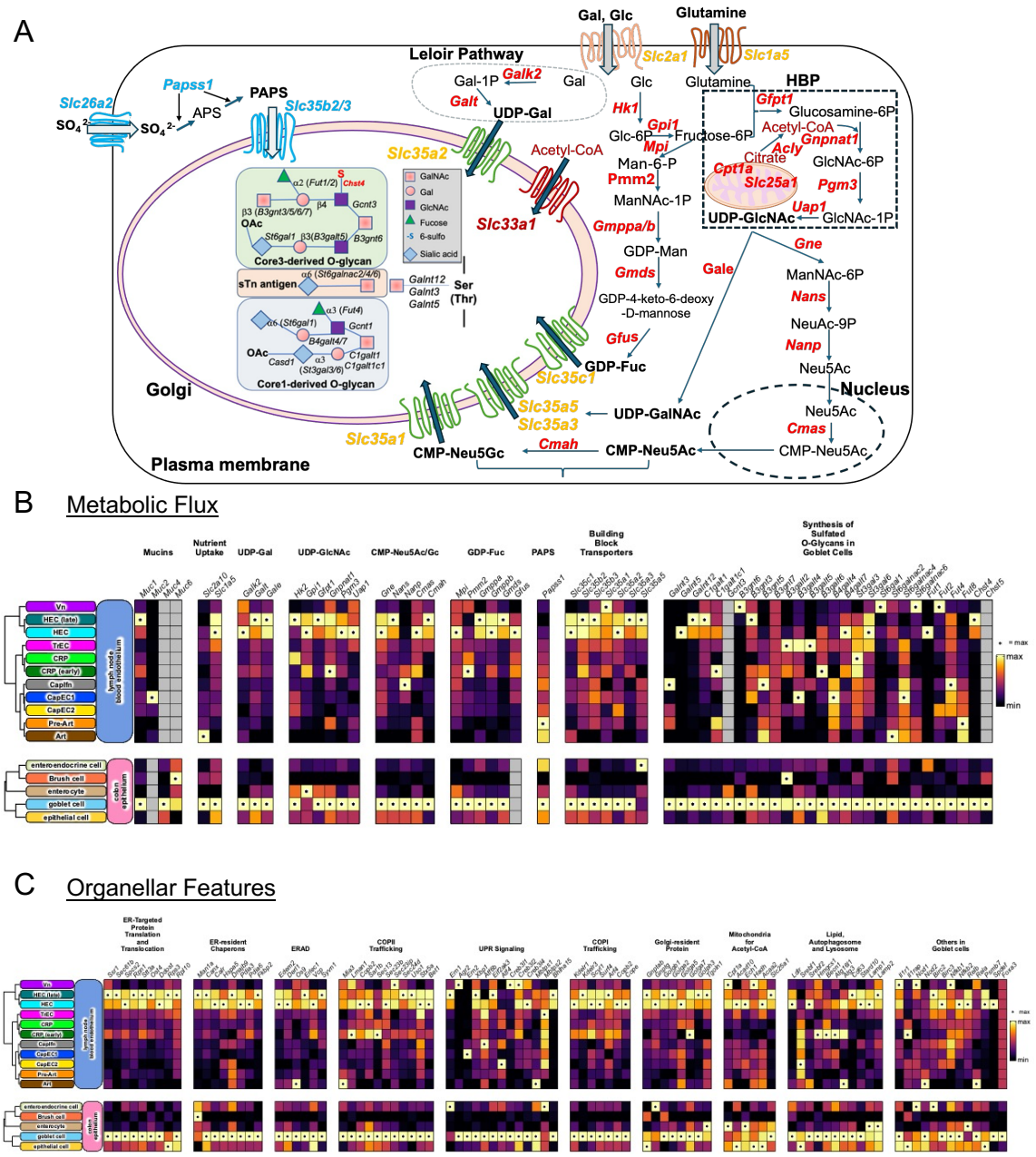

Suppl. Fig. 2. Goblet Cells Share Gene Programs with HECs to Drive Sulfated Mucin Production and Organelle Expansion (linked to Fig. 1). **A.** A schematic chart illustrates the progression of metabolic fluxes, beginning with nutrient uptake and the production of building blocks, followed by the intramembrane transport of building blocks, and culminating in the biosynthetic assembly of sulfated O-glycans within the Golgi apparatus in GCs. The fluxes are regulated by specific transporters and enzymes encoded by the genes highlighted in yellow and red, respectively, with those specifically involved in sulfation shown in blue. **B and C.** Heat maps display the GC enriched expression of genes involved in regulating the metabolic fluxes for sulfated musin biosynthesis (B) and organellar protein machineries (C). Mean expression values in panels C and F are derived from three independent samples and are shown on a color scale from min to max, with an asterisk (*) indicating the maximum value.

Supplemental Fig.3

A

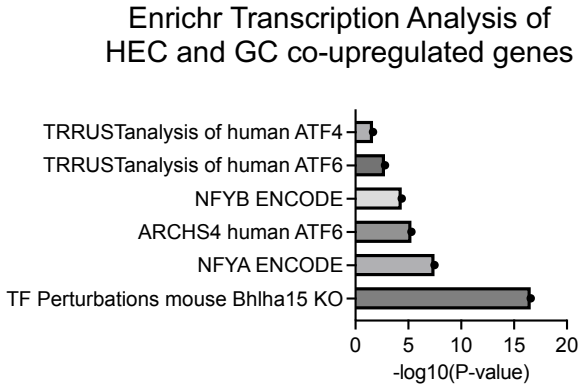

B

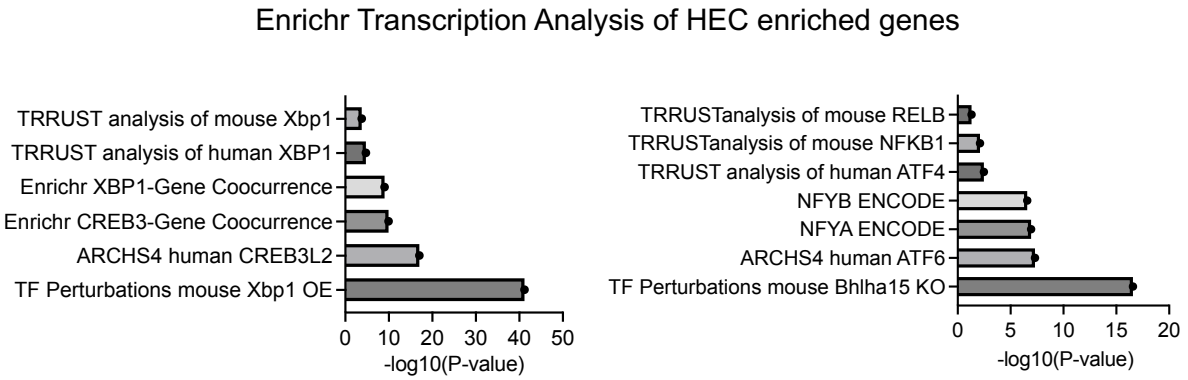

C

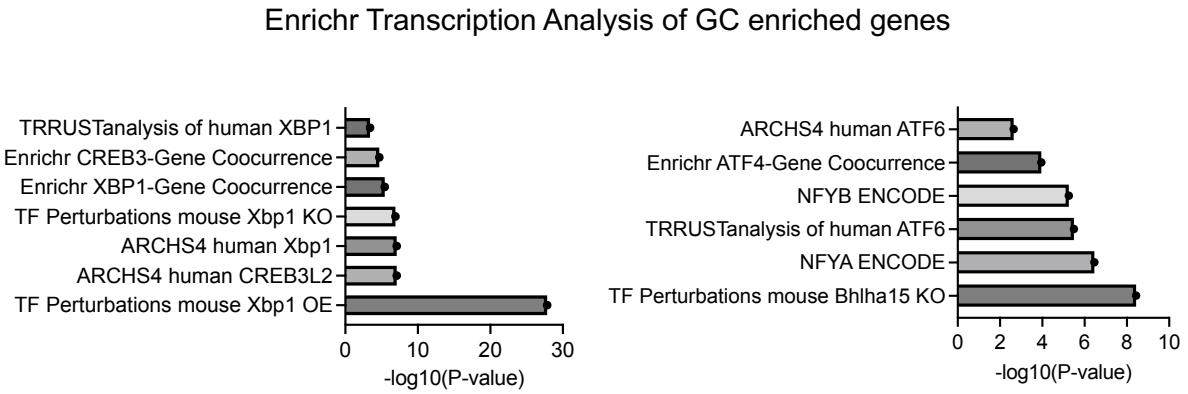

Suppl. Fig 3. (Linked to Figure 2). **A**. Enrichr TF analysis of the up-regulated DEGs common to HEC and GC (Data S2). **B.** Enrichr TF analysis of HEV enriched genes. **C.** Enrichr TF analysis of intestinal GC enriched genes (Data S3-4).

Supplemental Fig.4

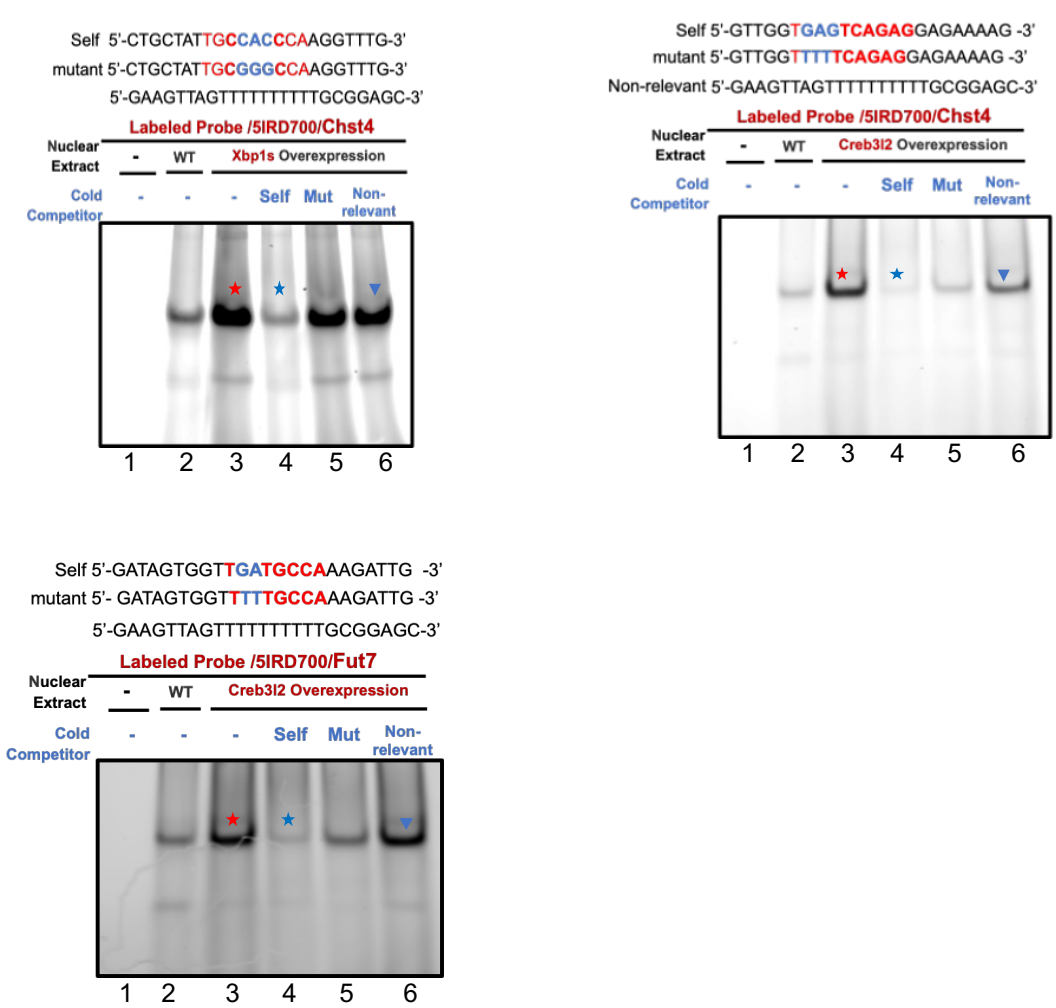

Suppl. Fig 4. EMSA Reveals Site-Specific Binding of Xbp1s and Creb3l2 to Target Motifs (Linked to Figure 3). **A**. Binding of recombinant XBP1s (left) and CREB3L2 (right) to the indicated labeled *Chst4* motif probes. The binding is specifically inhibited by addition of 100 excess of unlabeled wild-type, but not of mutant or nonrelevant probes. **B.** Binding of recombinant CREB3L2 to the indicated labeled *Fut7* motif probe. (A–B) Nuclear extracts were prepared from 293T cells transfected with expression vectors for recombinant XBP1s or CREB3L2. Extracts from wild type (WT) 293T as control. Lanes, from left to right: (1) Labeled probe without nuclear extract; (2) Labeled probe with WT control nuclear extract; (3) Labeled probe with nuclear extract from XBP1s-overexpressing cells (A, left) or CREB3L2-overexpressing cells (A, right; B) (red star); (4–6) Labeled probes incubated with the respective overexpressing nuclear extracts in the presence of 100-fold excess of unlabeled wild-type competitor probe (blue star, 4), mutant competitor (5), or irrelevant competitor (blue arrowhead, 6). Results shown are representative of three independent experiments.

Supplemental Fig.5

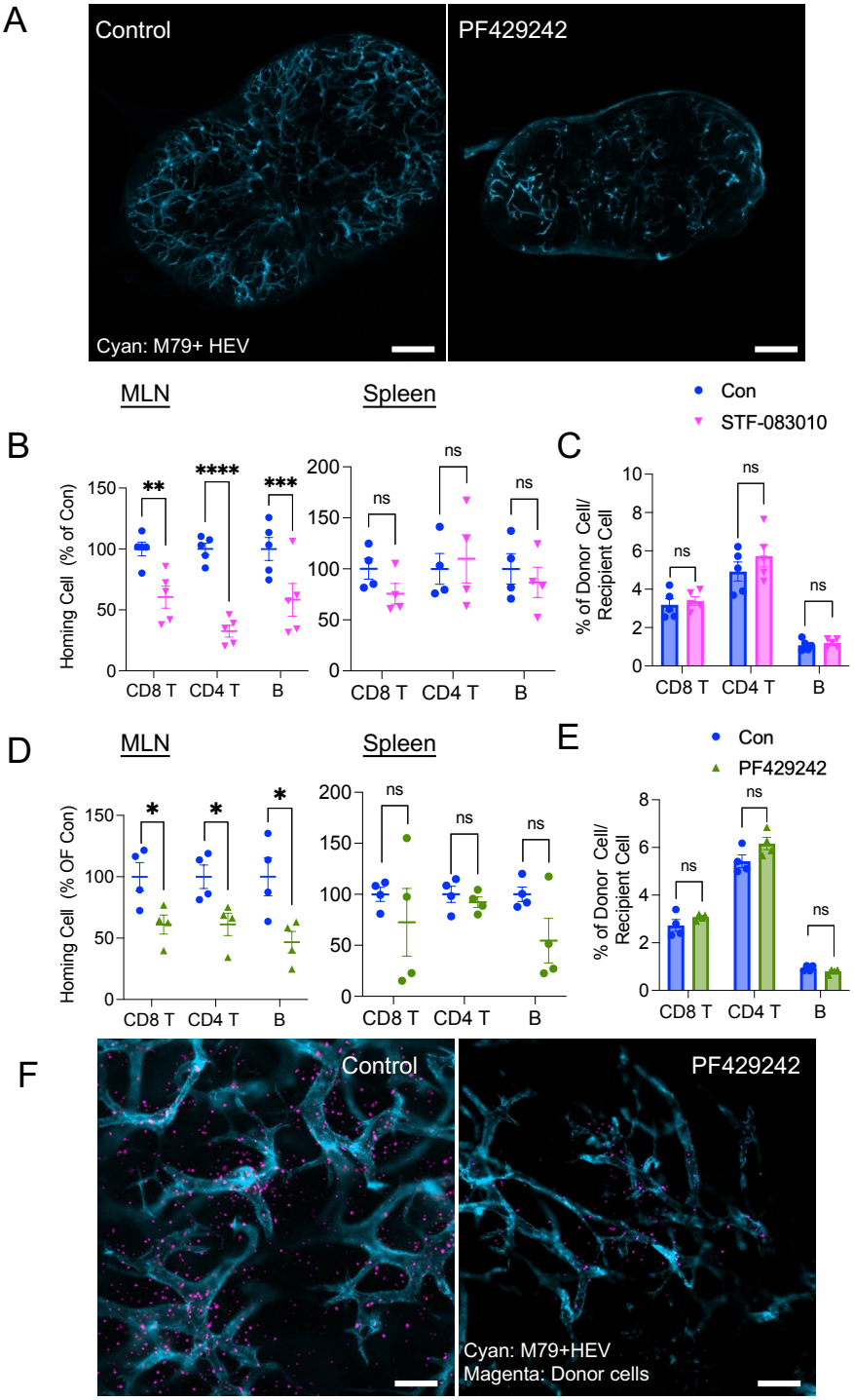

Suppl. Fig. 5. (Linked to Figure 4) **A.** Representative whole-mount IF images of PLNs from mice treated with Creb3l2 inhibitor PF429242 or control, stained with i.v. injected antibodies: anti-PNAd (blue); anti-CD31 not shown. Scale bar: 500 µm.
B, D. Localization of donor lymphocytes in MLN and spleen 2 hours after homing in mice treated with STF-083010 (B) or PF429242 (D), compared to controls. Data represent the percentage of the mean localization ratio relative to WT.
C, E. Donor-to-recipient cell ratios in PLNs from mice treated with STF-083010 (C) or PF429242 (E).
F. Representative IF images showing short-term (30 min) diapedesis in control and PF429242-treated mice. Staining includes anti-PNAd and CFSE-labeled donor cells. Scale bar: 100 µm.
B–E: Results are pooled data (mean ± SEM) of n=5 or 4 mice per group. Statistical significance was assessed using paired two-tailed t-tests. *p < 0.05; **p < 0.01; ***p < 0.001; ****p < 0.0001.

Supplemental Fig.6

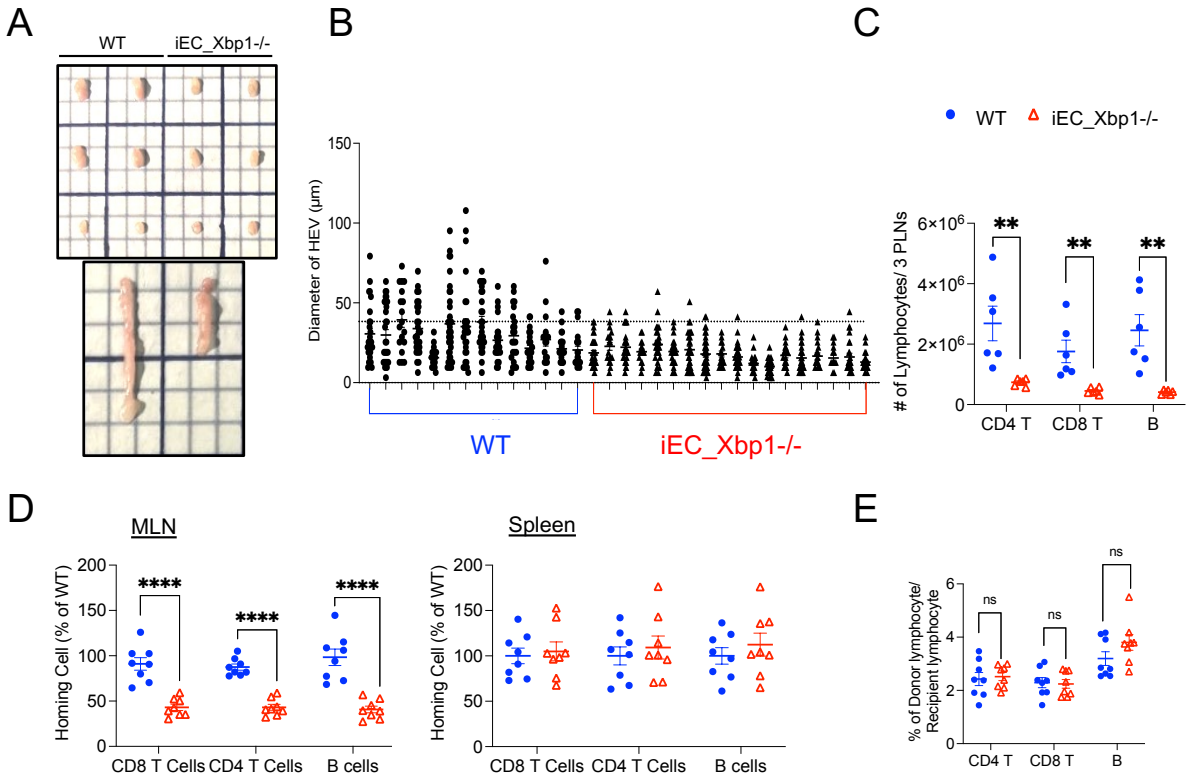

Suppl. Fig. 6. (Linked to Figure 5)**. A.** Representative images of LNs. Upper panel: from top to bottom—inguinal PLN, axillary PLN, and brachial PLN. Lower panel: MLN. **B**. Quantification of HEV diameter. Data represent 14–35 measurements per 10X field (~4 mm²/field), averaged from 2–3 representative fields per PLN, with 1–2 PLNs analyzed per mouse (n = 5 mice per group). Results are shown as mean ± SEM. **C.** Lymphocytes counts from 3 pooled PLNs (Inguinal, Axillary, and Branchial PLN) per mouse. n=5 per group. **D.** Localization of donor lymphocytes in MLN and spleen from control and *Xbp1* deficient mice after 2-hour short-term homing assay. Data are shown as a percentage of the mean localization ratio relative to the WT group. **F**. Quantification of percentage of donor lymphocyte per recipient lymphocyte in the short-term homing assay. (F and H): Shown are data (mean ± SEM) with 8 mice per group. Two-tailed paired t-tests were used for all comparisons. *: p value<0.05;**: p value<0.01; ***: p value < 0.001. ****: p value < 0.0001.

Supplemental Fig.7

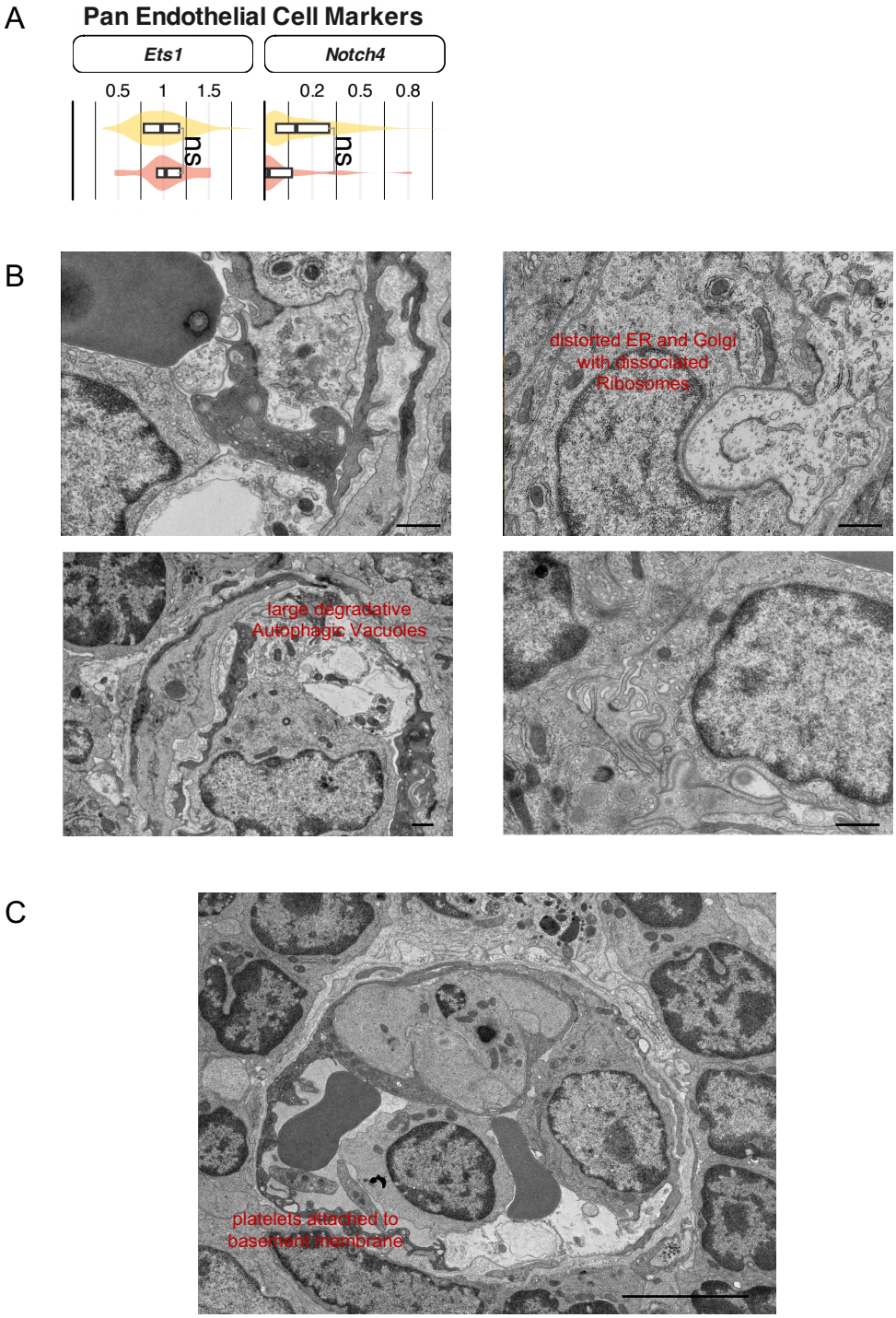

Suppl. Fig. 7. (Linked to Figure 6)**. A.** scRNA-seq analysis of HECs from WT and iEC_Xbp1^{-}/$^{-}$ mice shows that expression of pan-endothelial markers, such as Ets1 and Notch4, remains unchanged. **B.** scRNA-seq analysis comparing WT and Xbp1KO HECs. Results displayed using Enrichr or UMAP (Vaccenic Plot). Scale bars: 800 nm. **C.** Representative high-magnification TEM images of Xbp1KO HECs. N: nucleus. Left: Platelets attached to the basement membrane. Middle: Large degradative autophagic vacuoles. Right: Distorted ER and Golgi with dissociated ribosomes. Scale bars: 5 μm.

Reference

1. Palm, W., and Thompson, C.B. (2017). Nutrient acquisition strategies of mammalian cells. Nature *546*, 234-242. 10.1038/nature22379.
2. Jackson, B.T., and Finley, L.W.S. (2024). Metabolic regulation of the hallmarks of stem cell biology. Cell Stem Cell *31*, 161-180. 10.1016/j.stem.2024.01.003.
3. Buck, M.D., Sowell, R.T., Kaech, S.M., and Pearce, E.L. (2017). Metabolic Instruction of Immunity. Cell *169*, 570-586. 10.1016/j.cell.2017.04.004.
4. Chapman, N.M., and Chi, H. (2022). Metabolic adaptation of lymphocytes in immunity and disease. Immunity *55*, 14-30. 10.1016/j.immuni.2021.12.012.
5. Li, X., Sun, X., and Carmeliet, P. (2019). Hallmarks of Endothelial Cell Metabolism in Health and Disease. Cell Metab *30*, 414-433. 10.1016/j.cmet.2019.08.011.
6. von Andrian, U.H., and Mempel, T.R. (2003). Homing and cellular traffic in lymph nodes. Nat Rev Immunol *3*, 867-878. 10.1038/nri1222.
7. Butcher, E.C., and Picker, L.J. (1996). Lymphocyte homing and homeostasis. Science *272*, 60-66. 10.1126/science.272.5258.60.
8. Rosen, S.D. (2004). Ligands for L-selectin: homing, inflammation, and beyond. Annu Rev Immunol *22*, 129-156. 10.1146/annurev.immunol.21.090501.080131.
9. Streeter, P.R., Rouse, B.T., and Butcher, E.C. (1988). Immunohistologic and functional characterization of a vascular addressin involved in lymphocyte homing into peripheral lymph nodes. J Cell Biol *107*, 1853-1862. 10.1083/jcb.107.5.1853.
10. Anderson, N.D., Anderson, A.O., and Wyllie, R.G. (1976). Specialized structure and metabolic activities of high endothelial venules in rat lymphatic tissues. Immunology *31*, 455-473.
11. Mebius, R.E., Streeter, P.R., Breve, J., Duijvestijn, A.M., and Kraal, G. (1991). The influence of afferent lymphatic vessel interruption on vascular addressin expression. J Cell Biol *115*, 85-95. 10.1083/jcb.115.1.85.
12. Gustafsson, J.K., and Johansson, M.E.V. (2022). The role of goblet cells and mucus in intestinal homeostasis. Nat Rev Gastroenterol Hepatol *19*, 785-803. 10.1038/s41575-022-00675-x.
13. Ruddle, N.H. (2023). Regulation, Maintenance, and Remodeling of High Endothelial Venules in Homeostasis, Inflammation, and Cancer. Curr Opin Physiol *36*. 10.1016/j.cophys.2023.100705.
14. Vella, G., Hua, Y., and Bergers, G. (2023). High endothelial venules in cancer: Regulation, function, and therapeutic implication. Cancer Cell *41*, 527-545. 10.1016/j.ccell.2023.02.002.
15. Meza-Perez, S., and Randall, T.D. (2017). Immunological Functions of the Omentum. Trends Immunol *38*, 526-536. 10.1016/j.it.2017.03.002.
16. Browning, J.L., Allaire, N., Ngam-Ek, A., Notidis, E., Hunt, J., Perrin, S., and Fava, R.A. (2005). Lymphotoxin-beta receptor signaling is required for the homeostatic control of HEV differentiation and function. Immunity *23*, 539-550. 10.1016/j.immuni.2005.10.002.
17. Sun, S.C. (2017). The non-canonical NF-kappaB pathway in immunity and inflammation. Nat Rev Immunol *17*, 545-558. 10.1038/nri.2017.52.
18. Blanchard, L., and Girard, J.P. (2021). High endothelial venules (HEVs) in immunity, inflammation and cancer. Angiogenesis *24*, 719-753. 10.1007/s10456-021-09792-8.
19. Scheper, A.F., Schofield, J., Bohara, R., Ritter, T., and Pandit, A. (2023). Understanding glycosylation: Regulation through the metabolic flux of precursor pathways. Biotechnol Adv *67*, 108184. 10.1016/j.biotechadv.2023.108184.

20. Schjoldager, K.T., Narimatsu, Y., Joshi, H.J., and Clausen, H. (2020). Global view of human protein glycosylation pathways and functions. Nat Rev Mol Cell Biol *21*, 729-749. 10.1038/s41580-020-00294-x.
21. Walter, P., and Ron, D. (2011). The unfolded protein response: from stress pathway to homeostatic regulation. Science *334*, 1081-1086. 10.1126/science.1209038.
22. Bettigole, S.E., and Glimcher, L.H. (2015). Endoplasmic reticulum stress in immunity. Annu Rev Immunol *33*, 107-138. 10.1146/annurev-immunol-032414-112116.
23. Khan, H.A., and Margulies, C.E. (2019). The Role of Mammalian Creb3-Like Transcription Factors in Response to Nutrients. Front Genet *10*, 591. 10.3389/fgene.2019.00591.
24. Fox, R.M., and Andrew, D.J. (2015). Transcriptional regulation of secretory capacity by bZip transcription factors. Front Biol (Beijing) *10*, 28-51. 10.1007/s11515-014-1338-7.
25. Lee, M., Kiefel, H., LaJevic, M.D., Macauley, M.S., Kawashima, H., O'Hara, E., Pan, J., Paulson, J.C., and Butcher, E.C. (2014). Transcriptional programs of lymphoid tissue capillary and high endothelium reveal control mechanisms for lymphocyte homing. Nat Immunol *15*, 982-995. 10.1038/ni.2983.
26. Brulois, K., Rajaraman, A., Szade, A., Nordling, S., Bogoslowski, A., Dermadi, D., Rahman, M., Kiefel, H., O'Hara, E., Koning, J.J., et al. (2020). A molecular map of murine lymph node blood vascular endothelium at single cell resolution. Nat Commun *11*, 3798. 10.1038/s41467-020-17291-5.
27. Veerman, K., Tardiveau, C., Martins, F., Coudert, J., and Girard, J.P. (2019). Single-Cell Analysis Reveals Heterogeneity of High Endothelial Venules and Different Regulation of Genes Controlling Lymphocyte Entry to Lymph Nodes. Cell Rep *26*, 3116-3131 e3115. 10.1016/j.celrep.2019.02.042.
28. Paneque, A., Fortus, H., Zheng, J., Werlen, G., and Jacinto, E. (2023). The Hexosamine Biosynthesis Pathway: Regulation and Function. Genes (Basel) *14*. 10.3390/genes14040933.
29. Pietrocola, F., Galluzzi, L., Bravo-San Pedro, J.M., Madeo, F., and Kroemer, G. (2015). Acetyl coenzyme A: a central metabolite and second messenger. Cell Metab *21*, 805-821. 10.1016/j.cmet.2015.05.014.
30. Holden, H.M., Rayment, I., and Thoden, J.B. (2003). Structure and function of enzymes of the Leloir pathway for galactose metabolism. J Biol Chem *278*, 43885-43888. 10.1074/jbc.R300025200.
31. Gunal, S., Hardman, R., Kopriva, S., and Mueller, J.W. (2019). Sulfation pathways from red to green. J Biol Chem *294*, 12293-12312. 10.1074/jbc.REV119.007422.
32. Hirschberg, C.B., Robbins, P.W., and Abeijon, C. (1998). Transporters of nucleotide sugars, ATP, and nucleotide sulfate in the endoplasmic reticulum and Golgi apparatus. Annu Rev Biochem *67*, 49-69. 10.1146/annurev.biochem.67.1.49.
33. Gemmer, M., and Forster, F. (2020). A clearer picture of the ER translocon complex. J Cell Sci *133*. 10.1242/jcs.231340.
34. Wiseman, R.L., Mesgarzadeh, J.S., and Hendershot, L.M. (2022). Reshaping endoplasmic reticulum quality control through the unfolded protein response. Mol Cell *82*, 1477-1491. 10.1016/j.molcel.2022.03.025.
35. Benyair, R., Ogen-Shtern, N., and Lederkremer, G.Z. (2015). Glycan regulation of ER-associated degradation through compartmentalization. Semin Cell Dev Biol *41*, 99-109. 10.1016/j.semcdb.2014.11.006.
36. Robinson, C.M., Duggan, A., and Forrester, A. (2024). ER exit in physiology and disease. Front Mol Biosci *11*, 1352970. 10.3389/fmolb.2024.1352970.
37. Dell'Angelica, E.C., and Bonifacino, J.S. (2019). Coatopathies: Genetic Disorders of Protein Coats. Annu Rev Cell Dev Biol *35*, 131-168. 10.1146/annurev-cellbio-100818-125234.

38. Muschalik, N., and Munro, S. (2018). Golgins. Curr Biol *28*, R374-R376. 10.1016/j.cub.2018.01.006.
39. Guertin, D.A., and Wellen, K.E. (2023). Acetyl-CoA metabolism in cancer. Nat Rev Cancer *23*, 156-172. 10.1038/s41568-022-00543-5.
40. Debnath, J., Gammoh, N., and Ryan, K.M. (2023). Autophagy and autophagy-related pathways in cancer. Nat Rev Mol Cell Biol *24*, 560-575. 10.1038/s41580-023-00585-z.
41. Tan, S.L., Gale, M.J., Jr., and Katze, M.G. (1998). Double-stranded RNA-independent dimerization of interferon-induced protein kinase PKR and inhibition of dimerization by the cellular P58IPK inhibitor. Mol Cell Biol *18*, 2431-2443. 10.1128/MCB.18.5.2431.
42. Shaffer, A.L., Shapiro-Shelef, M., Iwakoshi, N.N., Lee, A.H., Qian, S.B., Zhao, H., Yu, X., Yang, L., Tan, B.K., Rosenwald, A., et al. (2004). XBP1, downstream of Blimp-1, expands the secretory apparatus and other organelles, and increases protein synthesis in plasma cell differentiation. Immunity *21*, 81-93. 10.1016/j.immuni.2004.06.010.
43. Abo, H., Muraki, A., Harusato, A., Imura, T., Suzuki, M., Takahashi, K., Denning, T.L., and Kawashima, H. (2023). N-acetylglucosamine-6-O sulfation on intestinal mucins prevents obesity and intestinal inflammation by regulating gut microbiota. JCI Insight *8*. 10.1172/jci.insight.165944.
44. Asada, R., Saito, A., Kawasaki, N., Kanemoto, S., Iwamoto, H., Oki, M., Miyagi, H., Izumi, S., and Imaizumi, K. (2012). The endoplasmic reticulum stress transducer OASIS is involved in the terminal differentiation of goblet cells in the large intestine. J Biol Chem *287*, 8144-8153. 10.1074/jbc.M111.332593.
45. Neidhardt, L., Cloots, E., Friemel, N., Weiss, C.A.M., Harding, H.P., McLaughlin, S.H., Janssens, S., and Ron, D. (2024). The IRE1beta-mediated unfolded protein response is repressed by the chaperone AGR2 in mucin producing cells. EMBO J *43*, 719-753. 10.1038/s44318-023-00014-z.
46. Brandl, K., Rutschmann, S., Li, X., Du, X., Xiao, N., Schnabl, B., Brenner, D.A., and Beutler, B. (2009). Enhanced sensitivity to DSS colitis caused by a hypomorphic Mbtps1 mutation disrupting the ATF6-driven unfolded protein response. Proc Natl Acad Sci U S A *106*, 3300-3305. 10.1073/pnas.0813036106.
47. Kuleshov, M.V., Jones, M.R., Rouillard, A.D., Fernandez, N.F., Duan, Q., Wang, Z., Koplev, S., Jenkins, S.L., Jagodnik, K.M., Lachmann, A., et al. (2016). Enrichr: a comprehensive gene set enrichment analysis web server 2016 update. Nucleic Acids Res *44*, W90-97. 10.1093/nar/gkw377.
48. Xie, Z., Bailey, A., Kuleshov, M.V., Clarke, D.J.B., Evangelista, J.E., Jenkins, S.L., Lachmann, A., Wojciechowicz, M.L., Kropiwnicki, E., Jagodnik, K.M., et al. (2021). Gene Set Knowledge Discovery with Enrichr. Curr Protoc *1*, e90. 10.1002/cpz1.90.
49. Hinrichs, A.S., Karolchik, D., Baertsch, R., Barber, G.P., Bejerano, G., Clawson, H., Diekhans, M., Furey, T.S., Harte, R.A., Hsu, F., et al. (2006). The UCSC Genome Browser Database: update 2006. Nucleic Acids Res *34*, D590-598. 10.1093/nar/gkj144.
50. Siepel, A., Bejerano, G., Pedersen, J.S., Hinrichs, A.S., Hou, M., Rosenbloom, K., Clawson, H., Spieth, J., Hillier, L.W., Richards, S., et al. (2005). Evolutionarily conserved elements in vertebrate, insect, worm, and yeast genomes. Genome Res *15*, 1034-1050. 10.1101/gr.3715005.
51. Zoonomia, C. (2020). A comparative genomics multitool for scientific discovery and conservation. Nature *587*, 240-245. 10.1038/s41586-020-2876-6.
52. Heinz, S., Benner, C., Spann, N., Bertolino, E., Lin, Y.C., Laslo, P., Cheng, J.X., Murre, C., Singh, H., and Glass, C.K. (2010). Simple combinations of lineage-determining transcription factors prime cis-regulatory elements required for macrophage and B cell identities. Mol Cell *38*, 576-589. 10.1016/j.molcel.2010.05.004.
53. Stray-Pedersen, A., Backe, P.H., Sorte, H.S., Morkrid, L., Chokshi, N.Y., Erichsen, H.C., Gambin, T., Elgstoen, K.B., Bjoras, M., Wlodarski, M.W., et al. (2014). PGM3 mutations

cause a congenital disorder of glycosylation with severe immunodeficiency and skeletal dysplasia. Am J Hum Genet *95*, 96-107. 10.1016/j.ajhg.2014.05.007.
54. van Karnebeek, C.D.M., Bonafe, L., Wen, X.Y., Tarailo-Graovac, M., Balzano, S., Royer-Bertrand, B., Ashikov, A., Garavelli, L., Mammi, I., Turolla, L., et al. (2017). Corrigendum: NANS-mediated synthesis of sialic acid is required for brain and skeletal development. Nat Genet *49*, 969. 10.1038/ng0617-969a.
55. Wood, S.A., Park, J.E., and Brown, W.J. (1991). Brefeldin A causes a microtubule-mediated fusion of the trans-Golgi network and early endosomes. Cell *67*, 591-600. 10.1016/0092-8674(91)90533-5.
56. Hawkins, J.L., Robbins, M.D., Warren, L.C., Xia, D., Petras, S.F., Valentine, J.J., Varghese, A.H., Wang, I.K., Subashi, T.A., Shelly, L.D., et al. (2008). Pharmacologic inhibition of site 1 protease activity inhibits sterol regulatory element-binding protein processing and reduces lipogenic enzyme gene expression and lipid synthesis in cultured cells and experimental animals. J Pharmacol Exp Ther *326*, 801-808. 10.1124/jpet.108.139626.
57. Cao, Z.J., You, J., Fan, Y.M., Yang, J.Y., Sun, J., Ma, X., Zhang, J., Li, Z., Wang, X., and Feng, Y.X. (2025). Noncanonical UPR factor CREB3L2 drives immune evasion of triple-negative breast cancer through Hedgehog pathway modulation in T cells. Sci Adv *11*, eads5434. 10.1126/sciadv.ads5434.
58. Papandreou, I., Denko, N.C., Olson, M., Van Melckebeke, H., Lust, S., Tam, A., Solow-Cordero, D.E., Bouley, D.M., Offner, F., Niwa, M., and Koong, A.C. (2011). Identification of an Ire1alpha endonuclease specific inhibitor with cytotoxic activity against human multiple myeloma. Blood *117*, 1311-1314. 10.1182/blood-2010-08-303099.
59. Lin, J.C., Liu, T.P., Chen, Y.B., and Yang, P.M. (2023). PF-429242 exhibits anticancer activity in hepatocellular carcinoma cells via FOXO1-dependent autophagic cell death and IGFBP1-dependent anti-survival signaling. Am J Cancer Res *13*, 4125-4144.
60. Yeh, J.C., Hiraoka, N., Petryniak, B., Nakayama, J., Ellies, L.G., Rabuka, D., Hindsgaul, O., Marth, J.D., Lowe, J.B., and Fukuda, M. (2001). Novel sulfated lymphocyte homing receptors and their control by a Core1 extension beta 1,3-N-acetylglucosaminyltransferase. Cell *105*, 957-969. 10.1016/s0092-8674(01)00394-4.
61. Liu, W., Xiong, W., Liu, W., Hirakawa, J., and Kawashima, H. (2023). A novel monoclonal antibody against 6-sulfo sialyl Lewis x glycans attenuates murine allergic rhinitis by suppressing Th2 immune responses. Sci Rep *13*, 15740. 10.1038/s41598-023-43017-w.
62. Dinh, T.T., Xiang, M., Rajaraman, A., Wang, Y., Salazar, N., Zhu, Y., Roper, W., Rhee, S., Brulois, K., O'Hara, E., et al. (2022). An NKX-COUP-TFII morphogenetic code directs mucosal endothelial addressin expression. Nat Commun *13*, 7448. 10.1038/s41467-022-34991-2.
63. Ballet, R., Brennan, M., Brandl, C., Feng, N., Berri, J., Cheng, J., Ocon, B., Alborzian Deh Sheikh, A., Marki, A., Bi, Y., et al. (2021). A CD22-Shp1 phosphatase axis controls integrin beta(7) display and B cell function in mucosal immunity. Nat Immunol *22*, 381-390. 10.1038/s41590-021-00862-z.
64. Sorensen, I., Adams, R.H., and Gossler, A. (2009). DLL1-mediated Notch activation regulates endothelial identity in mouse fetal arteries. Blood *113*, 5680-5688. 10.1182/blood-2008-08-174508.
65. Hetz, C., Lee, A.H., Gonzalez-Romero, D., Thielen, P., Castilla, J., Soto, C., and Glimcher, L.H. (2008). Unfolded protein response transcription factor XBP-1 does not influence prion replication or pathogenesis. Proc Natl Acad Sci U S A *105*, 757-762. 10.1073/pnas.0711094105.
66. Kawashima, H., Petryniak, B., Hiraoka, N., Mitoma, J., Huckaby, V., Nakayama, J., Uchimura, K., Kadomatsu, K., Muramatsu, T., Lowe, J.B., and Fukuda, M. (2005). N-acetylglucosamine-6-O-sulfotransferases 1 and 2 cooperatively control lymphocyte

homing through L-selectin ligand biosynthesis in high endothelial venules. Nat Immunol *6*, 1096-1104. 10.1038/ni1259.
67. Welch, L.G., Peak-Chew, S.Y., Begum, F., Stevens, T.J., and Munro, S. (2021). GOLPH3 and GOLPH3L are broad-spectrum COPI adaptors for sorting into intra-Golgi transport vesicles. J Cell Biol *220*. 10.1083/jcb.202106115.
68. Kumar, V., Chyou, S., Stein, J.V., and Lu, T.T. (2012). Optical projection tomography reveals dynamics of HEV growth after immunization with protein plus CFA and features shared with HEVs in acute autoinflammatory lymphadenopathy. Front Immunol *3*, 282. 10.3389/fimmu.2012.00282.
69. Tzeng, T.C., Chyou, S., Tian, S., Webster, B., Carpenter, A.C., Guaiquil, V.H., and Lu, T.T. (2010). CD11c(hi) dendritic cells regulate the re-establishment of vascular quiescence and stabilization after immune stimulation of lymph nodes. J Immunol *184*, 4247-4257. 10.4049/jimmunol.0902914.
70. Choi, J., Sutaria, N., Roh, Y.S., Bordeaux, Z., Alphonse, M.P., Kwatra, S.G., and Kwatra, M.M. (2021). Translational Relevance of Mouse Models of Atopic Dermatitis. J Clin Med *10*. 10.3390/jcm10040613.
71. Rangel-Moreno, J., Moyron-Quiroz, J.E., Carragher, D.M., Kusser, K., Hartson, L., Moquin, A., and Randall, T.D. (2009). Omental milky spots develop in the absence of lymphoid tissue-inducer cells and support B and T cell responses to peritoneal antigens. Immunity *30*, 731-743. 10.1016/j.immuni.2009.03.014.
72. Yoshihara, T., and Okabe, Y. (2023). Aldh1a2 + fibroblastic reticular cells regulate lymphocyte recruitment in omental milky spots. J Exp Med *220*. 10.1084/jem.20221813.
73. Okabe, Y. (2024). Development and organization of omental milky spots. Immunol Rev *324*, 68-77. 10.1111/imr.13337.
74. Middleton, J., Americh, L., Gayon, R., Julien, D., Mansat, M., Mansat, P., Anract, P., Cantagrel, A., Cattan, P., Reimund, J.M., et al. (2005). A comparative study of endothelial cell markers expressed in chronically inflamed human tissues: MECA-79, Duffy antigen receptor for chemokines, von Willebrand factor, CD31, CD34, CD105 and CD146. J Pathol *206*, 260-268. 10.1002/path.1788.
75. Qian, C.N., Berghuis, B., Tsarfaty, G., Bruch, M., Kort, E.J., Ditlev, J., Tsarfaty, I., Hudson, E., Jackson, D.G., Petillo, D., et al. (2006). Preparing the "soil": the primary tumor induces vasculature reorganization in the sentinel lymph node before the arrival of metastatic cancer cells. Cancer Res *66*, 10365-10376. 10.1158/0008-5472.CAN-06-2977.
76. Martinet, L., Garrido, I., Filleron, T., Le Guellec, S., Bellard, E., Fournie, J.J., Rochaix, P., and Girard, J.P. (2011). Human solid tumors contain high endothelial venules: association with T- and B-lymphocyte infiltration and favorable prognosis in breast cancer. Cancer Res *71*, 5678-5687. 10.1158/0008-5472.CAN-11-0431.
77. Drayton, D.L., Liao, S., Mounzer, R.H., and Ruddle, N.H. (2006). Lymphoid organ development: from ontogeny to neogenesis. Nat Immunol *7*, 344-353. 10.1038/ni1330.
78. Habtezion, A., Nguyen, L.P., Hadeiba, H., and Butcher, E.C. (2016). Leukocyte Trafficking to the Small Intestine and Colon. Gastroenterology *150*, 340-354. 10.1053/j.gastro.2015.10.046.
79. Hansson, G.C. (2020). Mucins and the Microbiome. Annu Rev Biochem *89*, 769-793. 10.1146/annurev-biochem-011520-105053.
80. Grey, M.J., De Luca, H., Ward, D.V., Kreulen, I.A., Bugda Gwilt, K., Foley, S.E., Thiagarajah, J.R., McCormick, B.A., Turner, J.R., and Lencer, W.I. (2022). The epithelial-specific ER stress sensor ERN2/IRE1beta enables host-microbiota crosstalk to affect colon goblet cell development. J Clin Invest *132*. 10.1172/JCI153519.
81. Kaser, A., Lee, A.H., Franke, A., Glickman, J.N., Zeissig, S., Tilg, H., Nieuwenhuis, E.E., Higgins, D.E., Schreiber, S., Glimcher, L.H., and Blumberg, R.S. (2008). XBP1 links ER

stress to intestinal inflammation and confers genetic risk for human inflammatory bowel disease. Cell *134*, 743-756. 10.1016/j.cell.2008.07.021.
82. Johnson, D.M., Wells, M.B., Fox, R., Lee, J.S., Loganathan, R., Levings, D., Bastien, A., Slattery, M., and Andrew, D.J. (2020). CrebA increases secretory capacity through direct transcriptional regulation of the secretory machinery, a subset of secretory cargo, and other key regulators. Traffic *21*, 560-577. 10.1111/tra.12753.

Methods

Mice

Xbp1^{tm2Glm} mice[1] (provided by Dr. Jonathan Lin from Stanford University) were crossed with CDH5(PAC) Cre^{ERT2} mice[2] to generate tamoxifen-inducible endothelial cell-specific Xbp1 knockout (KO) mice (Cre+ Xbp1$^{f/f}$; iEC-Xbp1-/-). Littermates not harboring the Cre transgene were used as controls. Tamoxifen (75 mg/kg, Sigma-Aldrich, CAS # 10540-29-1) was administered via intraperitoneal (i.p.) injection four times, every other day, except for the omentum study, where tamoxifen was administered orally by gavage at the same dose. Wild-type (WT) C57BL/6J mice were obtained from the Jackson Laboratory (Bar Harbor, USA). Tamoxifen was prepared in corn oil at a concentration of 20 mg/ml by shaking overnight at 37°C in a light-protected vessel and stored at 4°C for the duration of the injections. Both male and female mice aged 6–20 weeks were used in experiments. Animals were housed under standard conditions (12 h/12 h light/dark cycle, 22 ± 2°C) with ad libitum access to food and tap water. All protocols discussed in the text and below have been approved or meet the guidelines of the accredited Department of Laboratory Animal Medicine and the Administrative Panel on Laboratory Animal Care at the VA Palo Alto Health Care System (VAPAHCS). Animals were sacrificed using approved procedures.

Preparation of lymphoid tissue BECs and flow cytometry

Axillary, inguinal, and brachial peripheral lymph nodes (PLNs) from 10–20 adult mice were dissociated as previously described[3,4]. To minimize technical variation, male and female PLN samples were combined prior to processing. Post-sequencing, the samples were computationally separated using the **AddModuleScore** function in the Seurat package (v3.1.1), leveraging the enrichment of male-specific Y-chromosomal genes and the female-specific gene *Xist*. Endothelial cells (ECs) were isolated following the procedure outlined in the **online protocol**[3]. Briefly, PLNs were pooled in HBSS buffer and minced with scissors. The tissue was washed 2–3 times with HBSS, then resuspended in HBSS containing 0.2 mg/ml collagenase P, 0.8 mg/ml Dispase II, and 0.01 mg/ml DNase. Samples were incubated at 37 °C for 10 minutes, followed by gentle disruption through repeated pipetting with P1000 pipette tips of successively smaller bore sizes. After allowing tissue fragments to settle, released cells were transferred into ice-cold FBS (final concentration, 30%). The remaining tissue was subjected to a second round of digestion with fresh buffer. Digested cells were filtered, and hematolymphoid cells were depleted using anti-CD45 MicroBeads (Miltenyi).

Isolated mouse ECs were surface-stained with monoclonal anti-mouse antibodies: APC-conjugated anti-CD31 (390; 102410; 1:4000), peridinin chlorophyll protein–cyanine 5.5–conjugated anti-CD45 (30-F11; 103131; 1:400), peridinin chlorophyll protein–cyanine

5.5–conjugated anti-Ter-119 (TER-119 TER-119; 116227; 1:400), peridinin chlorophyll protein–cyanine 5.5–conjugated anti-CD11a (H155-78; 141007; 1:400), peridinin chlorophyll protein–cyanine 5.5–conjugated anti-CD326 (G8.8; 118219; 1:400), phycoerythrin-cyanine 7-conjugated anti-Gp38 (8.1.1; 127411; 1:100), and APC/Cyanine7-conjugated anti-Ly6c (HK1.4; 128026, 1:200) (Biolegend). Anti-PNAd (MECA79) were produced in-house from hybridomas; labelled with DyLight Antibody Labeling Kits and used at a concentration of 2mg/ml (1:400).
For additional barcoding, ECs from the PLNs of iEC-Xbp1-/- and control mice (4-5 weeks post- tamoxifen treatment) were further stained with TotalSeq™-A anti-mouse Hashtag antibodies (1:200) (BioLegend). Dead cells were excluded by staining with 4',6-diamidino-2-phénylindole (DAPI) or the LIVE/DEAD Fixable Aqua dye (Invitrogen).
Approximately 5–10 × 10^4 BECs ($lin^-Gp38^-CD31^+$) were sorted into 100% fetal bovine serum using a FACS Aria (100 µm nozzle; ~2500 cells/second). Freshly sorted cell suspensions were diluted with PBS to a final FBS concentration of ~10%, then centrifuged at 400 × g for 5 minutes. The supernatant was carefully removed using micropipettes, and the cell pellets were resuspended in the residual volume (~30–50 µl). Cells were counted using a hemocytometer, and the concentration was adjusted to 500–1000 cells/µl by adding PBS with 10% FBS, if necessary.

Single-cell RNA sequencing

Single-cell gene expression was measured using the 10x Chromium v3 platform with the Chromium Single Cell 3' Library and Gel Bead Kit v2 (10X Genomics, PN-120237), following the manufacturer's guidelines. Male and female cohorts were processed together and computationally resolved post-sequencing. Libraries were sequenced on an Illumina NextSeq 500 using the 150-cycle High Output V2 Kit (Read 1: 26 bases, Read 2: 98 bases, Index 1: 8 bases). The Cell Ranger package (v6.0.1) was used to align high-quality reads to the mm10 transcriptome. Quality control and data analysis were performed as described previously7. Briefly, normalized log expression values were calculated using the scran package8. Imputed expression values were generated using a customized implementation of the MAGIC algorithm9 (Markov Affinity-based Graph Imputation of Cells) with optimized parameters (t = 2, k = 9, ka = 3) available at https://github.com/kbrulois/magicBatch.
Supervised cell selection was performed to exclude cells expressing non-blood endothelial gene signatures, including lymphatic endothelial cells (Prox1, Lyve1, Pdpn), pericytes (Itga7, Pdgfrb), fibroblastic reticular cells (Pdpn, Ccl19, Pdgfra), and lymphocytes (Ptprc, Cd52). The EC subsets clusters were identified based on canonical marker expression and their position in tSpace projections, yielding a total of 11 subsets7. Batch effects from technical replicates were corrected using the MNN algorithm as implemented in the batchelor package (v1.0.1) via the fastMNN function. Dimensionality reduction was performed using the UMAP algorithm. To account for cell-cycle effects, the data were split into dividing and resting cells, and the fastMNN function was used to align dividing cells with their resting counterparts. All subsets were represented by cells from both male and female mice across each condition. Heatmaps were created using the ComplexHeatmap package15, Cell subsets were clustered based on their mean expression profiles using ClustGeo and vegan packages. Violin plots were generated using the ggplot2 package, where y-axis units represent log-transformed normalized

counts following imputation. DEGs between selected blood endothelial7 and intestinal goblet cell subsets16 were determined using a two-sided Student's t-Test. Genes were considered differentially expressed if they met the following criteria: Average $\log_2$ fold change ($\log_2$FC) ≥ 0.0586 and a false discovery rate (FDR) ≤ 9.94×10^{-44}. The least significant DEG had a $-\log_{10}$(P) value of 47.30. The complete DEG list is provided in Table S1.

Cell lines

bEnd.3 and HEK293T cells were obtained from ATCC (CRL-2299 and CRL-3216 respectively). HEK293T cells were grown in Dulbecco's modified Eagle's medium (DMEM) containing high glucose and L-pyruvate and supplemented with 10% heat-inactivated fetal bovine serum, at 37 °C in 5%CO2. bEnd.3 and DN-MAML bEnd.3 cells were grown in the same media supplemented with penicillin-streptomycin[5]. Stable bEnd.3 cell transfectants overexpressing Fut7 promoter reporter were generated by transfection and selected with puromycin (1ug/ml).

Plasmid constructs

Chst4 enhancer-promoter and *Fut7* promoter fragments were PCR-amplified fragment from mouse genomic cDNA and cloned into pGL4.23[*luc2P*/Puro] and pGL4.22[*luc2P*/Puro] respectively to generate the luciferase (LUC) reporter constructs. pGL4.23[*luc2P*/Puro] and pGL4.22 [*luc2P*/Puro] vectors were obtained from Promega. *Pgm3*, *Nans*, and *Galt* enhancer-promoter_LUC reporter constructs were made by Vector Builder custom service. Control Renilla (Ren) Luciferase vector is from Promega.
For co-transfection studies, mammalian expression vectors un-spliced Xbp1 (Xbp1), spliced Xbp1 (Xbp1s), IRE1 dominant negative kinase mutant (IRE1-Mut), IRE1, Creb3l2 were commercially obtained. Constructs information is provided in Table S5.

Transient transfection

For luciferase reporter assays, 1.5×10^5 HEK293T cells were plated in 24-well plates and transfected upon reaching ~70–80% confluency. Respective luciferase reporters, transcription factors, and a Renilla luciferase control vector (Promega) were co-transfected using the Lipofectamine 3000 system (Thermo Fisher Scientific) according to the manufacturer's instructions. Forty-eight hours post-transfection, cells were lysed using Lysis Reagent (Promega). Firefly and Renilla luminescence were measured using the Dual-Glo® Luciferase Assay System and read with a Turner Biosystems 20/20n luminometer. Luciferase activity was quantified as the ratio of Firefly to Renilla luminescence.

Electrophoretic mobility shift assay (EMSA)

EMSAs were performed as previously described[5,6]. Double-stranded, fluorescence-labeled, and unlabeled probes were generated by annealing sense and antisense oligonucleotides (Sequences shown in Supplemental Fig. 4). Each binding reaction contained 1–2 pmol of labeled probe and 50 µg of nuclear extracts from 293T cells expressing recombinant spliced Xbp1 or CREB3L2. Gel shift reactions were conducted at 4 °C for 1 hour in 1.875 mg poly(d1-dC),100 mM NaCl, 10 mM Tris, 1 mM DTT, 1 mM EDTA, Protease inhibitors (1:1000), 1% BSA. In reactions with cold competitors, 50-fold

molar excess of ("cold") competitor unlabeled probes were added. Protein–probe complexes were separated on 5% Mini-PROTEAN® TBE gels (Bio-Rad) run in 4% TBE buffer (Bio-Rad). Gels were imaged using the Odyssey Imaging System (LI-COR).

Pharmacological inhibition of IRE1α-Xbp1 and Creb3l2

For the pharmacological inhibition of IRE1α-Xbp1, WT C57BL/6J mice were injected with STF-083010 (30 mg/kg, i.p.) or DMSO, both given in 16% (vol/vol) Cremophor EL (Sigma-Aldrich) saline solution via i.p. injections every other day for four does[7]. For inhibiting active Creb3l2, WT C57BL/6J mice were administrated with PF-429242 (20 mg/kg, i.v.) or saline solution daily for two weeks[8,9].

Imaging

Peripheral lymph nodes (PLNs), omentum, and ear skin were imaged following retroorbital injection of fluorescently labeled antibodies. Antibodies (10–25 μg) were administered 20–30 minutes prior to sacrifice and tissue collection. To visualize the overall vasculature, tissues were gently compressed to a thickness of approximately 35–50 μm on a glass slide. Imaging was performed using a Zeiss LSM 880 laser scanning microscope and a Nikon ECLIPSE Ti2 microscope.

Image quantification

The parameter characterization and quantification of images were analyzed in Imaris 9.1. Parameters assessed included number of total units of individual cell-size particles expressing specific fluorescence signals and volumetric surface area, representing the external surface area of an isosurface. Individual CFSE-stained cells were identified and counted using the "Spots" module. Volumetric measurements for Ly6c$^+$, MECA-79$^+$, and CD31$^+$ structures were obtained by creating 3D isosurfaces based on fluorescence detection via the "Surfaces" module. Statistics for total surface area, total volume were generated by the software and exported as CSV files for further calculations and statistical analysis. For analysis of cells within high endothelial venules (HEVs), a mask was applied to exclude voxels inside the region of interest (ROI), allowing quantification of cell distributions external to the surface objects, also utilizing the "Spots" module.

Short-term homing and short-term diapedesis assays

Donor splenocytes were isolated and were labeled with 2.5 μM CFSE (Invitrogen) or CellTrace Yellow dye (Invitrogen) for 15 min at 37°C in RPMI without fetal bovine serum (FBS). A total of 50–100 × 10^6 donor cells were transferred into recipient mice (wild-type mice, wild-type mice treated with inhibitors, and iEC-Xbp1$^{-/-}$ mice) via retroorbital injection.

For the homing assay, peripheral lymph nodes (PLNs; pooled axillary, inguinal, and brachial nodes; average of 3 PLNs per mouse), mesenteric lymph nodes (MLNs), Peyer's patches (PPs; average of 3 per mouse), and spleens were harvested 2 hours after donor cell injection. Single-cell suspensions were surface-stained for flow cytometry using the following monoclonal antibodies: PC-conjugated anti-CD4 (RM4-5; 100516; 1:200), BV421-conjugated anti-CD8β (YTS156.7.7; 126629; 1:200), PE-Cy7-conjugated anti-CD3 (145-2C11; 100320; 1:200), PE-conjugated anti-CD19 (6D5; 115508; 1:200), and

FITC-conjugated anti-IgD (11.26c.2a; 11-5993-82; 1:100). Appropriate isotype controls were included. The Fc receptors were blocked using Rat Serum and anti-CD16/32 prior to the staining. Dead cells were excluded using Fixable Aqua Dead Cell Stain (Invitrogen), and counting beads were added to determine absolute cell numbers. T and B cell homing efficiencies were calculated as the ratio of recovered cells to input cells and normalized relative to the mean ratio of the wild-type control group.

For the diapedesis assay, tissues were collected 30 minutes after donor cell injection. Fluorescently labeled antibodies (10–25 µg) were administered retroorbitally 15 minutes prior to sacrifice. To visualize the overall vasculature, tissues were gently compressed to a thickness of approximately 35–50 µm on a glass slide. Imaging was performed using an LSM 880 laser scanning microscope (Zeiss) and an ECLIPSE Ti2 microscope (Nikon).

Delayed-Type Hypersensitivity (DTH) Assay

The DTH reaction in WT and iEC-Xbp1^{-}/$^{-}$ mice was induced as previously described[10]. Briefly, the DTH response was triggered through repeated epicutaneous application of 2,4-dinitrofluorobenzene (DNFB; Sigma-Aldrich). Primary immunization was achieved by applying 0.5% DNFB (50 µL in acetone: olive oil, 4:1) to bare abdominal skin on Day 1. On Day 7, mice were challenged by applying 0.5% DNFB (20 µL) to both sides of the left ear to elicit a secondary DTH response, while the right ear received 20 µL of solvent (acetone: olive oil, 4:1) as a control. 24 hours post-challenge, the thickness of both the left and right ears was measured with Ames calipers. The inflamed skin along with the draining lymph nodes (auricular and inguinal LNs) was harvested for FACS and H&E analysis.

Preparation of lymphocytes from skin and flow cytometry

Skin-infiltrating T cells were released from the connective tissue after separating the epidermal sheets as described[10-12]. T cells were surface-stained with monoclonal anti-mouse antibodies for flow cytometry, including BV421-conjugated anti-CD4 (RM4-5, 100563, 1:200); PE-Cy7-conjugated anti-CD3 (145-2C11; 100320; 1:200); BV650-conjugated anti-CD45Rb (C363-16A; 740449; 1:150); APC-conjugated anti-CD44 (IM7; 560567; 1:2000). The Fc receptors were blocked using Rat Serum and anti-CD16/32 prior to the staining. Fixable Aqua dye was applied for live/dead cell staining, and counting beads were included to calculate absolute cell numbers.

Transmission Electron Microscopy

One inguinal lymph node from each wild-type or iEC-Xbp1^{-}/$^{-}$ mice was isolated and washed with cold PBS. The whole lymph nodes were fixed in Karnovsky's fixative: 2% Glutaraldehyde (EMS Cat# 16000) and 4% formaldehyde (EMS Cat# 15700) in 0.1M Sodium Cacodylate (EMS Cat# 12300) pH 7.4 for 1 hr. then placed on ice 24 hours. The fix was replaced with cold/aqueous 1% Osmium tetroxide (EMS Cat# 19100) and were then allowed to warm to Room Temperature (RT) for 2 hrs rotating in a hood, washed 3X with ultrafiltered water, then en bloc stained in 1% Uranyl Acetate at RT 2hrs while rotating. Samples were then dehydrated in a series of ethanol washes for 30 minutes each @ RT beginning at 50%, 70% EtOH then moved to 4°C overnight. They were place in cold 95% EtOH and allowed to warm to RT, changed to 100% 2X, then Propylene

Oxide (PO) for 15 min. Samples are infiltrated with EMbed-812 resin (EMS Cat#14120) mixed 1:2, 1:1, and 2:1 with PO for 2 hrs each with leaving samples in 2:1 resin to PO overnight rotating at RT in the hood. The samples are then placed into EMbed-812 for 2 to 4 hours then placed into molds w/labels and fresh resin, orientated and placed into 65° C oven overnight.
Sections were taken around 80nm using an UC7 (Leica, Wetzlar, Germany) picked up on formvar/Carbon coated 100-mesh copper grids, stained for 40seconds in 3.5% Uranyl Acetate in 50% Acetone followed by staining in Sato's Lead Citrate for 2 minutes. Observed in the JEOL JEM-1400 120kV. Images were taken using a Gatan OneView 4k X 4k digital camera.

Lymph node and Ear immunization

Mice underwent a cutaneous immune challenge by applying 20 µL of 3–5% 4-Ethoxymethylene-2-phenyl-2-oxazolin-5-one (Sigma–Aldrich) dissolved in a 1:2 acetone:oil mixture. For lymph node analysis, the solution was applied to bare abdominal skin, while for skin analysis, it was applied to both sides of the ears. Peripheral lymph nodes (axillary, brachial, and inguinal) were collected on Day 4, and ear tissues were harvested on Day 10 following inflammation induction for imaging purposes.

HEV induction in Omentum

Six-week-old iEC-Xbp1^{-}/$^{-}$ and control mice were administered tamoxifen (75 mg/kg) orally via gavage every other day for a total of four doses. Four to five weeks after tamoxifen treatment, mice received LPS (5 mg/kg) intraperitoneally twice over a 72-hour period, followed by omentum vasculature imaging.

De novo TF motif search

Regulatory regions of HEV-enriched genes, which include the gene body and the 5 kb upstream and downstream regions, were intersected with regions with log-odds score greater than 300 in UCSC Genome Browser's phastCons Placental Elements track, which aligns 60 vertebrate species and measures evolutionary conservation of genomic sequences[13,14] De novo TF motif search was performed for conserved regulatory regions of HEV-enriched genes in the mouse mm10 genome using HOMER[15]. All conserved regions of HEV genes are provided as a custom track in a UCSC Genome Browser session: https://genome.ucsc.edu/s/m.xiang/HEV_genes_conserved.

TF regulation analysis

List of HEC and GC co-upregulated DEGs, HEC- and GC- enriched genes were analyzed to identify candidate upstream TF regulators using Enrichr[16-18]. Results of TF regulators from select databases are shown. Detailed analysis, including the gene lists used, is provided in Data 2-4.

Comparative Genomics and Phylogenomic Analysis

Comparative genomics and phylogenetic footprinting were performed using the UCSC Genome Browser to identify evolutionarily constrained regions across candidate genes, including promoter regions, 5′ and 3′ untranslated regions (UTRs), and intronic sequences. Analyses were based on the 58 eutherian mammals Multiz Alignment and

PhyloP Basewise Conservation tracks to evaluate sequence conservation. To identify putative transcriptional regulatory elements, we utilized the TFBS Conserved track and the JASPAR TFBS database, focusing on conserved binding motifs for XBP1 and CREB3L2 within the identified regulatory modules.

Data and statistical analysis

Results are expressed as mean ± SEM and individual data points represent biological replicates. Statistics were calculated using GraphPad Prism, with differences among means tested for statistical significance as indicated in the corresponding figure legend. Statistical significance is indicated by the following: *P ≤ 0.05, **P ≤ 0.01, ***P ≤ 0.001 and ****P≤0.0001. No statistical significance is denoted as 'na'.

Reference

1. Hetz, C., Lee, A.H., Gonzalez-Romero, D., Thielen, P., Castilla, J., Soto, C., and Glimcher, L.H. (2008). Unfolded protein response transcription factor XBP-1 does not influence prion replication or pathogenesis. Proc Natl Acad Sci U S A *105*, 757-762. 10.1073/pnas.0711094105.
2. Sorensen, I., Adams, R.H., and Gossler, A. (2009). DLL1-mediated Notch activation regulates endothelial identity in mouse fetal arteries. Blood *113*, 5680-5688. 10.1182/blood-2008-08-174508.
3. Lee, M., Kiefel, H., LaJevic, M.D., Macauley, M.S., Kawashima, H., O'Hara, E., Pan, J., Paulson, J.C., and Butcher, E.C. (2014). Transcriptional programs of lymphoid tissue capillary and high endothelium reveal control mechanisms for lymphocyte homing. Nat Immunol *15*, 982-995. 10.1038/ni.2983.
4. Brulois, K., Rajaraman, A., Szade, A., Nordling, S., Bogoslowski, A., Dermadi, D., Rahman, M., Kiefel, H., O'Hara, E., Koning, J.J., et al. (2020). A molecular map of murine lymph node blood vascular endothelium at single cell resolution. Nat Commun *11*, 3798. 10.1038/s41467-020-17291-5.
5. Dinh, T.T., Xiang, M., Rajaraman, A., Wang, Y., Salazar, N., Zhu, Y., Roper, W., Rhee, S., Brulois, K., O'Hara, E., et al. (2022). An NKX-COUP-TFII morphogenetic code directs mucosal endothelial addressin expression. Nat Commun *13*, 7448. 10.1038/s41467-022-34991-2.
6. Bi, Y., Shi, X., Zhu, J., Guan, X., Garbacz, W.G., Huang, Y., Gao, L., Yan, J., Xu, M., Ren, S., et al. (2018). Regulation of Cholesterol Sulfotransferase SULT2B1b by Hepatocyte Nuclear Factor 4alpha Constitutes a Negative Feedback Control of Hepatic Gluconeogenesis. Mol Cell Biol *38*. 10.1128/MCB.00654-17.
7. Papandreou, I., Denko, N.C., Olson, M., Van Melckebeke, H., Lust, S., Tam, A., Solow-Cordero, D.E., Bouley, D.M., Offner, F., Niwa, M., and Koong, A.C. (2011). Identification of an Ire1alpha endonuclease specific inhibitor with cytotoxic activity against human multiple myeloma. Blood *117*, 1311-1314. 10.1182/blood-2010-08-303099.
8. Lin, J.C., Liu, T.P., Chen, Y.B., and Yang, P.M. (2023). PF-429242 exhibits anticancer activity in hepatocellular carcinoma cells via FOXO1-dependent autophagic cell death and IGFBP1-dependent anti-survival signaling. Am J Cancer Res *13*, 4125-4144.

9. Wang, T.B., Geng, M., Jin, H., Tang, A.G., Sun, H., Zhou, L.Z., Chen, B.H., Shen, G., and Sun, Q. (2021). SREBP1 site 1 protease inhibitor PF-429242 suppresses renal cell carcinoma cell growth. Cell Death Dis *12*, 717. 10.1038/s41419-021-03999-9.
10. Reiss, Y., Proudfoot, A.E., Power, C.A., Campbell, J.J., and Butcher, E.C. (2001). CC chemokine receptor (CCR)4 and the CCR10 ligand cutaneous T cell-attracting chemokine (CTACK) in lymphocyte trafficking to inflamed skin. J Exp Med *194*, 1541-1547. 10.1084/jem.194.10.1541.
11. Benck, C.J., Martinov, T., Fife, B.T., and Chatterjea, D. (2016). Isolation of Infiltrating Leukocytes from Mouse Skin Using Enzymatic Digest and Gradient Separation. J Vis Exp, e53638. 10.3791/53638.
12. Kunkel, E.J., Campbell, J.J., Haraldsen, G., Pan, J., Boisvert, J., Roberts, A.I., Ebert, E.C., Vierra, M.A., Goodman, S.B., Genovese, M.C., et al. (2000). Lymphocyte CC chemokine receptor 9 and epithelial thymus-expressed chemokine (TECK) expression distinguish the small intestinal immune compartment: Epithelial expression of tissue-specific chemokines as an organizing principle in regional immunity. J Exp Med *192*, 761-768. 10.1084/jem.192.5.761.
13. Hinrichs, A.S., Karolchik, D., Baertsch, R., Barber, G.P., Bejerano, G., Clawson, H., Diekhans, M., Furey, T.S., Harte, R.A., Hsu, F., et al. (2006). The UCSC Genome Browser Database: update 2006. Nucleic Acids Res *34*, D590-598. 10.1093/nar/gkj144.
14. Siepel, A., Bejerano, G., Pedersen, J.S., Hinrichs, A.S., Hou, M., Rosenbloom, K., Clawson, H., Spieth, J., Hillier, L.W., Richards, S., et al. (2005). Evolutionarily conserved elements in vertebrate, insect, worm, and yeast genomes. Genome Res *15*, 1034-1050. 10.1101/gr.3715005.
15. Heinz, S., Benner, C., Spann, N., Bertolino, E., Lin, Y.C., Laslo, P., Cheng, J.X., Murre, C., Singh, H., and Glass, C.K. (2010). Simple combinations of lineage-determining transcription factors prime cis-regulatory elements required for macrophage and B cell identities. Mol Cell *38*, 576-589. 10.1016/j.molcel.2010.05.004.
16. Chen, E.Y., Tan, C.M., Kou, Y., Duan, Q., Wang, Z., Meirelles, G.V., Clark, N.R., and Ma'ayan, A. (2013). Enrichr: interactive and collaborative HTML5 gene list enrichment analysis tool. BMC Bioinformatics *14*, 128. 10.1186/1471-2105-14-128.
17. Kuleshov, M.V., Jones, M.R., Rouillard, A.D., Fernandez, N.F., Duan, Q., Wang, Z., Koplev, S., Jenkins, S.L., Jagodnik, K.M., Lachmann, A., et al. (2016). Enrichr: a comprehensive gene set enrichment analysis web server 2016 update. Nucleic Acids Res *44*, W90-97. 10.1093/nar/gkw377.
18. Xie, Z., Bailey, A., Kuleshov, M.V., Clarke, D.J.B., Evangelista, J.E., Jenkins, S.L., Lachmann, A., Wojciechowicz, M.L., Kropiwnicki, E., Jagodnik, K.M., et al. (2021). Gene Set Knowledge Discovery with Enrichr. Curr Protoc *1*, e90. 10.1002/cpz1.90.